INTERNATIONAL JOURNAL OF AUTOMOTIVE AND MECHANICAL ENGINEERING
ISSN: 2229-8649 e-ISSN: 2180-1606
VOLUME 23, ISSUE 1, 2026, 13367 - 13392
DOI: https://doi.org/10.15282/ijame.23.1.2026.16.1014

RESEARCH ARTICLE

Risk-aware buckling design of functionally graded porous beams via machine-learning surrogates and reliability analysis

Satyasaibaba Pitta [1]*, **Ranga Janardhana Ginka** [2], **Balakrishna Banavathu** [1]

[1]Department of Mechanical Engineering, University College of Engineering, JNTUK, Kakinada-533003, India.
[2]Department of Mechanical Engineering, Jawaharlal Nehru Technological University, Anantapur, Anantapuramu-515002, India.

Abstract – Functionally graded porous beams offer high stiffness-to-weight ratios, but their buckling strength is sensitive to induced porosity variability. Designers, therefore, need tools that are both fast and explicitly risk-aware. This study develops and validates an interpretable methodology that combines higher-order shear deformation theory, machine learning surrogates, and structural reliability analysis to support buckling design of functionally graded porous beams. Deterministic buckling responses are first generated using a higher-order shear deformation theory for two boundary conditions (simply supported and clamped-clamped), two slenderness ratios (L/h=10 and 40), geometric controls (taper and width), porosity indices $0<\alpha<0.3$, and two porosity patterns (Regular and Uneven). A gradient-boosted tree surrogate is then trained on the log-transformed dimensionless critical buckling load using five-fold cross-validation. Manufacturing variability in porosity is propagated through the surrogate via Monte Carlo simulation, and a companion First-order Reliability Method (FORM) in the porosity dimension provides efficient estimates of failure probability. Risk is summarized through domain-wise mean buckling capacity and Conditional Value-at-Risk (CVaR) at the 5% level ($CVaR_{5\%}$), from which risk-return frontiers and "knee" designs distinguish risk-neutral from risk-averse choices. The surrogate generalizes strongly (out-of-fold log coefficient of determination, R^2log=0.94; mean absolute error, MAE=2.7; mean absolute percentage error, MAPE=9.5%), while FORM tracks Monte Carlo with near-perfect concordance (average R^2=0.9997; MAE(P_f)=0.0005; MAPE=0.33%), with small, interpretable deviations confined to slender, simply supported beams with uneven porosity. Across all regions, clamped-clamped, regular, and thick beams systematically dominate both mean and lower tail performance. Knee designs typically incur only 1-2% loss in mean capacity while retaining 95-99% of the best attainable CvaR, providing a reliable basis for compact, risk-aware buckling design guidance.

Article History

Received	:	27 September 2025
Revised	:	28 January 2026
Accepted	:	04 February 2026
Published	:	14 March 2026

Keywords
Functionally graded porous beams
Buckling surrogate modelling
Reliability analysis
Conditional value-at-Risk
Risk-aware structural design

1. Introduction

Lightweight structures that deliver high stiffness and stability at minimal mass are central to contemporary aerospace, automotive, biomedical, and energy applications. Among the many architected materials proposed for this purpose, Functionally Graded Porous (FGP) beams have emerged as compelling building blocks because their spatially varying composition and porosity enable tailored stiffness and mass distribution without sharp material interfaces [1, 2]. When such components are slender and lightly built, buckling, rather than strength, often governs design. This reality places a high value on predictive tools that can reliably evaluate critical buckling loads across broad design spaces, even under the inevitable manufacturing variability introduced by grading strategies and pore morphology [3, 4]. Classical beam theories provide baseline physics and terminology for FGP members. From Euler-Bernoulli and Timoshenko formulations to Higher-order shear deformation theories (HSDT), these models have enabled extensive deterministic buckling studies of graded/porous beams and plates [5]. Although significant progress has been made in deterministic response prediction, real-world design decisions are rarely made with such certainty. Modern manufacturing routes such as powder metallurgy, additive manufacturing, and infiltration/casting hybrids introduce scatter in porosity index (α), gradient indices (P_x, P_z), and geometric features such as taper or width ratio. There is thus a need for more than a single predicted number, and risk metrics that quantify tail behavior (e.g., failure probabilities) and support risk-aware optimization when selecting among competing designs.

Building on these foundations, recent studies have refined deterministic predictions through rich kinematics and improved numerics, clarifying the choice and porosity patterns. Kannaiyan and Balasubramaniam [6] used HSDT to analyze bi-directional FGP beams across boundary conditions, clarifying how simultaneous axial and thickness-wise grading reshapes critical loads and mode shapes, providing evidence that realistic grading cannot be reduced to a single exponent without loss of accuracy. Jiao et al. [7] adopted a dual-mesh control domain method to study free vibration and buckling of a functionally graded beam (FGB), demonstrating that careful spatial discretization can reduce dispersion and stabilize eigenvalue predictions over wider slenderness ranges. From a theory standpoint, Nguyen [8] introduced an HSDT (for laminated composites) that captures shear in a way directly portable to graded-porous members, reinforcing the trend toward higher-order kinematics for accurate buckling of thick or graded sections. Plate/shell results have highlighted the role of porosity distributions. Aljadani [9] (quasi-3D theory) showed that even vs uneven porosity patterns materially alter thermal buckling of functionally graded plates, a methodologically close analogue that supports the decision to treat "Regular" and "Uneven" beam patterns as distinct design regions. Martins et al. [10] demonstrated reliability-based calibration for local buckling, tuning partial safety factors to meet target reliabilities. Their procedure underscores a

*CORRESPONDING AUTHOR | S. Pitta | ✉ satyasaibabapitta@gmail.com cultural shift where buckling design should be reported in terms of gradient and reliability indices rather than as a single nominal critical buckling load. Khoshgoftar and Akari [11] investigated the mechanical buckling behavior of FGP circular plates with radially varying porosity, employing first-order shear deformation theory to demonstrate the influence of pore distribution on critical load under uniform radial compression. Rebai and Tidjani [12] offered a comprehensive buckling study of functionally graded plates, clarifying the modeling choices and plate parameters that influence predicted critical buckling load. Nguyen [13] presented a Laguerre-function Ritz formulation for FGP curved beams, including bending, buckling, and vibration for connecting straight beam results to curved members used in practice. At smaller scales, Mirzaei et al. [14] treated bi-directional FGP microbeams, where porosity distribution and size-dependent effects bending/ buckling/ vibration responses, highlighting that grading pattern and scale effects materially shift stability maps.

Estimating these quantities across many regions is computationally heavy with full physics. Machine learning (ML) surrogates have become the practical engine for reliability at scale [15-17]. Palmeri and Laurenzi [18] developed neural surrogates for the nonlinear buckling of cold-formed members. These models reproduce finite element (FE) loads with high accuracy while cutting evaluation time from minutes to fractions of a second, exactly the kind of speed that turns thousands of Monte Carlo (MC) samples from prohibitive to routine. Eshaghi et al. [19] used ML methods to analyze FGP beams, comparing physics-informed neural networks and operator-learning strategies and demonstrated generalization across arbitrary porosity distributions and tractions. Degtyarev et al. [20] used Natural Gradient Boosting (NGBoost) to predict probabilistic resistance rather than just a means, signaling a turn toward uncertainty-aware surrogates that natively output distributions, a natural step for risk metrics like Conditional Value-at-Risk (CVaR). Kim and Royer [21] used skew normal buckling load distributions and embedded them in the optimization of a functionally graded shell. Once responses are fast to evaluate, risk measures can be evaluated to co-equal design objectives, revealing when mean optimal and tail robust designs diverge. Beyond point predictions, the design studies adopted explicit risk measures and reliability optimization. Robust and risk formulations are advanced for buckling, such as the lower bound, imperfect shell design and random field design optimization, highlighting the need for gradient index and tail metrics rather than single nominal loads [22, 23]. Yang et al. [24] proposed a surrogate-based, reliability-oriented buckling topology optimization under random field load uncertainty, proving that reliability constraints can be imposed efficiently when surrogates and stochastic representations are chosen carefully. Li et al. [25] articulated risk design via scenario generation, highlighting CVaR (and related buffered risk measures) as convex-friendly, decision-relevant criteria for engineering systems under hybrid uncertainties. Table 1 synthesizes, for each study, the system investigated, core methods, treatment of uncertainty and reliability, and the specific gap that remains relative to the present study.

Table 1. Representative studies on FGP buckling, reliability-based design, ML surrogates, and their relation to the present work

Study	System/focus	Methods	Uncertainty/ reliability treatment	Key finding	Gap relative to present work
Chinthalapudi et al. [1]	Buckling of bi-directional FGP tapered beams	HSDT-based mechanical model + Random Forest integration for discrete transport/buckling problems	Primarily deterministic; ML used to emulate mechanics, not to propagate aleatory porosity scatter	Shows that data-driven models can efficiently emulate HSDT buckling responses for FGP beams	Does not build a calibrated surrogate explicitly for buckling reliability, nor couple ML with First-order reliability method/MC or risk metrics such as CVaR across regimes.
Kannaiyan et al. [3]; Kannaiyan and Balasubramaniam [6]	Critical buckling of FGP beams via Kuhn-Tucker conditions	Higher-order shear theories with Karush Kuhn Tucker-based optimization and R implementation	Deterministic stability analysis; no random porosity or reliability index evaluation	Clarifies how grading and porosity patterns influence critical load and mode shapes	Provides deterministic buckling envelopes, but no ML surrogate, no failure probabilities, and no risk-return frontiers
Reedy et al. [2, 26]	Deflection, bending, and modal characteristics of FGP/FGB beams with variable cross-sections	Timoshenko / HSDT formulations, numerical schemes for beams with taper/variable sections	Uncertainty is not modeled; parameters treated as nominal	Establish the influence of gradation, porosity, and geometry on static/vibration responses of graded/porous beams	Focus on deflection/vibration; do not treat manufacturing variability, nor reliability-oriented buckling design
Bridjesh et al. [27,31]	Buckling of bi-directional porous FGP beams	HSDT analytical-numerical framework for bidirectional grading and porosity	Deterministic parametric studies: porosity index is a design variable, not a random field	Quantifies how bi-directional gradation and porosity alter non-dimensional critical buckling load	No machine-learning surrogate, no stochastic porosity, and no risk metrics (Pf, CVaR) for design selection

Table 1. Continued

Study	System/focus	Methods	Uncertainty/ reliability treatment	Key finding	Gap relative to present work
Nguyen [8]; Aljadani [9]; Khoshgoftar and Akari [11]; Rebai and Tidjani [12]; Mirzaei et al. [14]	Buckling of FGP plates, curved beams, circular plates and microbeams with porosity	Quasi-3D / HSDT / MSGT formulations for various geometries	Mostly deterministic; some work explores parametric sensitivity to porosity distributions	Show that even vs uneven (or radially graded) porosity significantly changes buckling and thermal stability	These works motivate treating “Regular” vs “Uneven” patterns separately, but they stop at deterministic or sensitivity analysis; no ML reliability or risk-aware maps
Martins et al. [10]	Reliability calibration of local buckling strength for pultruded glass fiber reinforced polymer columns	Structural reliability analysis and partial safety factor calibration	Full reliability framework: target β, Pf, and code-calibrated resistance factors	Demonstrates how reliability indices can inform buckling design codes	Not specific to FGP beams or porosity scatter; no ML surrogate, no CVaR-type tail metrics or domain-wise risk-return frontiers
Fan et al. [22]; Peng et al. [23]	Robust/risk design of variable stiffness shells and generic structures under random fields	Kriging-assisted active learning, robust optimization, random field uncertainties	Explicit robust and reliability-based optimization under parameter randomness	Show that surrogate-assisted reliability can manage random fields efficiently	Do not treat FGP buckling or porosity; risk measures and surrogates are not specialized to FGP beams nor to domain-wise risk-return guidance
Yang et al. [24]	Reliability buckling topology optimization under random load fields	Surrogate-based topology optimization with reliability constraints	Reliability constraints imposed via surrogate models for buckling	Proves that reliability-constrained buckling optimization is feasible with surrogates	Focuses on topology rather than graded porous beams; no CVaR/knee designs or practical domain-wise shortlists
Li et al. [25]	Risk design optimization under hybrid uncertainties	Scenario generation + genetic programming; CVaR and related buffered risk measures	Uses CVaR as a convex, decision-relevant risk measure	Establishes CVaR as a practical metric for engineering decision-making under uncertainty	No application to FGP buckling; does not integrate ML surrogates with FORM/MC on porosity-driven instability
Palmeri and Laurenzi [18]	Buckling performance of lightweight composite tubular masts	Neural-network buckling surrogate vs FE	Implicit treatment of uncertainty via surrogate; reliability not explicitly quantified	Shows that surrogates can reduce buckling evaluation time by orders of magnitude	Surrogates target deterministic buckling loads; no FORM coupling, no failure probabilities, and no risk-aware mapping
Eshaghi et al. [19]	Scientific ML for analysis of FGP beams	Physics-informed and operator-learning surrogates for FGP responses	Mainly deterministic generalization across porosity distributions and loading	Demonstrates that ML can learn rich FGP response spaces efficiently	Does not connect surrogates to reliability estimators (FORM/MC), nor define risk-aware frontiers or domain-wise knee designs
Degtyarev et al. [20]	Probabilistic resistance of cellular steel beams	NGBoost surrogate yielding full resistance distributions	Direct probabilistic prediction; resistance treated as random output	Illustrates the move from point predictions to probabilistic resistance surrogates	Not tailored to FGP buckling; no structured comparison of FORM vs MC or regime-wise risk-return analysis
Kim and Royer [21]	Data-driven buckling design of thin shells with imperfections	Gradient boosting + distributional modeling of buckling loads	Uses skew-normal distributions and embeds statistics in optimization	Shows that data-driven buckling surrogates can feed risk-aware optimization for shells	Focused on shell imperfection sensitivity; does not address FGP beams with porosity variability nor provide a unified ML-FORM-MC framework

Despite these advances, three gaps remain at the intersection of FGP mechanics, reliability and machine learning. First, existing buckling studies on FGP/FGB beams are almost exclusively deterministic and rarely propagate manufacturing variability in porosity and grading into explicit reliability or tail risk metrics, especially in a regime-wise (Clamped-clamped-CC vs Simply supported-SS; thick vs slender; Regular vs Uneven). Second, while ML surrogates and scientific ML have been used either to emulate graded beams or to accelerate generic reliability analysis, there is no integrated methodology that couples an HSDT-based FGP buckling model with a rigorously validated surrogate integrating both MC and FORM to deliver fast, interpretable reliability estimates across regimes. Third, risk-aware design tools such as CVaR, risk-return maps and "knee" selections are beginning to appear for other structural systems but have not yet been tailored to FGP beams with porosity variability or translated into domain-wise selection rules that practitioners can apply directly. The novelty of the present study is to introduce a reliability-aware ML methodology that couples a rigorously validated gradient-boosted surrogate for dimensionless critical buckling load (N_{cr}) with FORM and surrogate-accelerated MC to quantify failure probability and tail behavior. Elevates CVaR to quantify the lower tail of N_{cr}, complementing mean performance and aligning with reliability-oriented decision making, alongside expected (mean) critical buckling load, extracting risk-return frontiers and "knee" designs per domain (combination of support (CC/SS), aspect ratio (L/h), and porosity pattern) and turns these results into domain-specific design guidance (ranked shortlists and maps) that separates mean optimal from tail robust choices. The combination yields screen-fast, decision-grade reliability for FGP beams across supports, slenderness, geometry controls, and porosity patterns.

The aim of the present study is to develop and rigorously validate a fast, transparent ML surrogate for critical buckling across boundary conditions, slenderness levels, porosity patterns, and geometry types. The present study makes three main contributions, (i) It develops and rigorously validates a fast, transparent gradient boosted surrogate for the dimensionless critical buckling load of bi-directional FGP tapered beams across boundary conditions (SS/CC), slenderness levels (L/h=10,40), geometry controls (taper/width), porosity indices and Regular/Uneven patterns, building on an HSDT semi analytical model. (ii) It couples this surrogate with surrogate accelerated MC simulation and a companion FORM approximation in the porosity dimension to quantify, for each regime, failure probability and lower tail robustness via CVaR, and systematically benchmarks FORM against MC. (iii) It transforms these reliability outputs into decision-grade design tools by constructing domain-wise risk-return maps, identifying efficient frontiers and "knee" designs, and providing ranked shortlists that separate risk-neutral (mean optimal) from risk-averse (CVaR optimal) choices for FGP buckling design.

2. Materials and Methods

2.1 Mathematics of Functionally Graded Porous Taper Beam

2.1.1 Formulation of the beam

A bi-directional FGP tapered beam is formulated using an HSDT methodology so that transverse shear effects are captured. The metal and ceramic phases are treated as homogeneous, isotropic constituents with no interfacial mass transfer. Kinematics are linearized (small strains), where the transverse shear tractions diminish on the top and bottom surfaces. The through-thickness shear strain field is represented by a hyperbolic shape function to enforce equilibrium. Material properties (e.g., stiffness and Poisson ratio) vary smoothly along the length and thickness of the beam. Porosity is imparted via a scalar index with either uniform or graded distribution, and rotary inertia/warping is neglected where their influence on buckling is minimal.

Step 1: Geometry and kinematic assumptions

Geometry is parameterized by the span L, a linearly tapered thickness from h_1 to h_2 and width from b_1 to b_2. Taper and width ratios are encoded through the non-dimensional ratios $h_x = 1 - h_2/h_1$ and $b_x = 1 - b_2/b_1$. Bidirectional grading is controlled by independent indices along the beam axis and thickness, enabling coupled axial through thickness heterogeneity within the HSDT kinematics. The formulation is applied for SS and CC boundary conditions used throughout the study, which also define the validation and comparison regimes. The model of the FGP beam is presented in Figure 1.

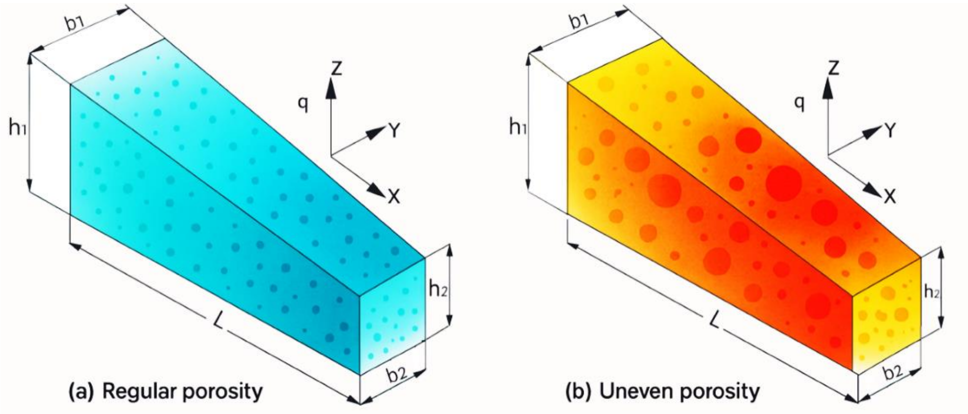

(a) Regular porosity (b) Uneven porosity

Figure 1. FGP beam model setup showing bidirectional grading, taper/width laws, porosity patterns (a) Regular and (b) Uneven) configurations

2.1.2 Material properties of functionally graded porous taper beam

The material gradation is prescribed in two spatial directions by volume fraction fields for the metal and ceramic phases, $V_m(x,z)$ and $V_c(x,z)$. The gradation laws use independent axial and thickness indices to capture bi-directional heterogeneity, while the thickness profile $h(x)$ accommodates non-linear taper and is defined within a symmetric axial coordinate frame. This construction preserves continuity through the thickness and admits realistic, non-uniform cross-sections.

Step 2: Bi-directional gradation and porosity modelling

The length of the beam is defined within a symmetrical axis coordinate system, where $x \in [0, L]$ and $z \in [-h(x)/2\, , +h(x)/2]$. The variation of volume fractions is shown in Eqs. (1) and (2) [26].

$$V_c(x,z) = \left(\frac{x}{L}\right)^{P_x}\left(\frac{1}{2}+\frac{z}{h(x)}\right)^{P_z} \tag{1}$$

$$V_m(x,z) + V_c(x,z) = 1 \tag{2}$$

where $V_m(x,z)$ and $V_c(x,z)$ are the volume fractions of metal (m) and ceramic (c), respectively. P_x and P_z are the gradient indices in the x and z directions, and $h(x)$ represents the thickness variations. The material gradation along the length of the beam is modelled by $\left(\frac{x}{L}\right)^{P_x}$ and $\left(\frac{1}{2}+\frac{z}{h(x)}\right)^{P_z}$ensures the symmetry and continuity in the thickness direction. $V_m(x,z)$ indirectly influences the transverse shear deformation by governing the effective material properties that are integrated into the HSDT through constitutive relations. The FGP beam exhibits continuous variation in its material properties throughout its thickness, which has the potential to be customized to attain specific attributes. The effective Young's modulus $E(x,z)$ and Poisson's ratio $\nu(x,z)$ of the FGP beam under even and uneven porosity distributions is calculated using Eqs. (3) to (6) [27].

$$E(x,z) = (E_c - E_m)\left(\frac{z}{h}+\frac{1}{2}\right)^{P_z}\left(\frac{x}{L}\right)^{P_x} + E_m - \frac{\alpha}{2}(E_c + E_m) \tag{3}$$

$$E(x,z) = (E_c - E_m)\left(\frac{z}{h}+\frac{1}{2}\right)^{P_z}\left(\frac{x}{L}\right)^{P_x} + E_m - \frac{\alpha}{2}(E_c + E_m)\left(1-\frac{2|z|}{h}\right) \tag{4}$$

$$\nu(x,z) = (\nu_c - \nu_m)\left(\frac{z}{h}+\frac{1}{2}\right)^{P_z}\left(\frac{x}{L}\right)^{P_x} + \nu_m - \frac{\alpha}{2}(\nu_c + \nu_m) \tag{5}$$

$$\nu(x,z) = (\nu_c - \nu_m)\left(\frac{z}{h}+\frac{1}{2}\right)^{P_z}\left(\frac{x}{L}\right)^{P_x} + \nu_m - \frac{\alpha}{2}(\nu_c + \nu_m)\left(1-\frac{2|z|}{h}\right) \tag{6}$$

where α is the porosity index ($0<\alpha<0.3$).

2.1.3 Strain-displacement relations

The strain-displacement relations link the longitudinal and transverse displacement fields to the corresponding measures of deformation. Strains are obtained from spatial gradients of the displacement field and include both normal and shear components, while displacements describe the motion of material points under load. Expressed as functions of the spatial coordinates, these relations form a core kinematic component of structural mechanics and highlight the analysis, design, and assessment of safe, efficient structures. Starting from the HSDT kinematics outlined in Section 2.1, the axial and transverse displacements are approximated by thickness expansion in terms of mid-plane quantities. The assumed displacement field takes the following form, which satisfies zero shear traction on the top and bottom surfaces and is compatible with the taper and grading described above.

Step 3: Strain-displacement and stress-resultant relations

The displacement field for the proposed FGP beam is presented in Eqs. (7) and (8) [28].

$$u(x,z) = u_0(x) + z\emptyset(x) - f(z)\left(\emptyset(x) + \frac{\partial w_0}{\partial x}(x)\right) \tag{7}$$

$$w(x,z) = w_0(x) \tag{8}$$

where $u(x,z)$ and $w(x,z)$ are the displacement fields in the x and z directions, respectively. $u_0(x)$ is the longitudinal displacement component, $\frac{\partial w_0}{\partial x}(x)$ is the effect of transverse displacement, w_0 is the transverse displacement, $f(z)$ is the shear shape function $\left(f\left(\pm\frac{h}{2}=0\right)\right) f$ and $\phi(x)$ is the variation in curvature along the length of the beam. Rotary inertia and warping are neglected for eigenvalue buckling. The mathematical equations representing the non-zero strains are shown in Eqs. (9) and (10) [29].

$$\varepsilon_x = \frac{\partial U}{\partial x} = \frac{\partial u_0}{\partial x} + z\frac{\partial \emptyset}{\partial x} - f(z)\left(\frac{\partial \emptyset}{\partial x} + \frac{\partial^2 w_0}{\partial x^2}\right) \tag{9}$$

$$\gamma_{xz} = \frac{\partial U}{\partial z} = \left[\emptyset(x) - f'(z)\left(\emptyset(x) + \frac{\partial w_0}{\partial x}(x)\right)\right] \tag{10}$$

ε_x is the normal strain in the longitudinal direction and γ_{xz} is the shear strain in the transverse direction. $f(z)$ [30] represents the shear shape function that characterizes the variation of transverse shear deformation across the height (z). The function is dependent on the thickness profile of the beam, which is described by h and is dependent on z.

$$f(z) = z - h\sinh\left(\frac{z}{\pi}\right) + zcosh\left(\frac{1}{2}\right) \tag{11}$$

$$f'(z) = 1 - hcosh\left(\frac{z}{\pi}\right)\left(\frac{1}{\pi}\right) + cosh\left(\frac{1}{2}\right) \tag{12}$$

In accordance with Hooke's law and using Eqs. (7) to (10), normal stress and shear stress are estimated using Eqs. (13) and (14).

$$\sigma_x = E(x)\varepsilon_x \tag{13}$$

$$\tau_{xz} = \frac{E(x)}{2(1+v)}\gamma_{xz} \tag{14}$$

where σ_x is the normal stress in the axial direction and τ_{xz} is the shear stress in the transverse direction. Eqs. (9)-(12) therefore express the normal and shear strains in terms of the generalized displacements, while Eqs. (13)-(14) map these strains into axial and shear stresses through the graded, porosity-dependent elastic moduli. These relations provide the local stress-strain description that enters the energy functional.

2.1.4 Constitutive equilibrium equations

Beginning with the principle of virtual work and incorporating the HSDT strain displacement relations, the equilibrium equations are derived. The governing field equations aggregate the effects of axial forces, shear forces, bending moments, and higher-order stress resultants intrinsic to the higher-order kinematics. The result is a coupled, generally nonlinear system of differential equations that provides the basis for the numerical solution.

Step 4: Energy functional, equilibrium equations, and buckling eigenproblem

The global equilibrium equations are obtained from the principle of virtual work by integrating the strain energy of the graded, tapered section and equating its variation to the virtual work of the external compressive load. The strain energy (∂U) denotes the elastic potential stored in the body due to deformation, the reversible work required to deform the material [31].

$$\partial U = \frac{1}{2}\int_0^L \int_{-\frac{h}{2}}^{+\frac{h}{2}} (\sigma_x\varepsilon_x + \tau_{xz}\gamma_{xz})dzdx \tag{15}$$

By substituting Eq. (7) to Eq. (12) in Eq. (15), the strain energy is derived as follows:

$$\partial U = \int_0^L \int_A \left\{\sigma_x\left[\frac{du_o}{dx} + 2\frac{d\emptyset}{dx} - f(z)\left(\frac{d\emptyset}{dx} + \frac{\partial^2 w_0}{\partial x^2}\right)\right] + \sigma_{xz}\left[\left(\frac{\partial w_0}{\partial x} + \emptyset - \left(z - h\sinh\left(\frac{z}{\pi}\right) + zcosh\left(\frac{1}{2}\right)\right)\left(\emptyset + \frac{\partial w_0}{\partial x}\right)\right)\right]\right\} dAdx \tag{16}$$

$$\begin{aligned}\partial U = \int_0^L \int_A \Bigg\{&\sigma_x\left[\frac{du_o}{dx} + 2\frac{d\emptyset}{dx} - \left(z - h\sinh\left(\frac{z}{\pi}\right) + zcosh\left(\frac{1}{2}\right)\right)\frac{d\emptyset}{dx} - \left(z - h\sinh\left(\frac{z}{\pi}\right) + zcosh\left(\frac{1}{2}\right)\right)\frac{\partial^2 w_0}{\partial x^2}\right] + \\ &\sigma_{xz}\left[\left(\frac{\partial w_0}{\partial x} + \emptyset - \left(z - h\sinh\left(\frac{z}{\pi}\right) + zcosh\left(\frac{1}{2}\right)\right)\emptyset - \left(z - h\sinh\left(\frac{z}{\pi}\right) + zcosh\left(\frac{1}{2}\right)\right)\frac{\partial w_0}{\partial x}\right)\right]\Bigg\} dAdx\end{aligned} \tag{17}$$

$$\begin{aligned}\partial U = \int_0^L \Bigg[&N_x\frac{du_0}{dx} + M_x\frac{d\emptyset}{dx} - \left[\frac{Cosh\left(\frac{1}{2}\right)\pi - hSinh\left(\frac{z}{\pi}\right) + \pi}{\pi}\right]P_x\frac{d\emptyset}{dx} - \left[\frac{Cosh\left(\frac{1}{2}\right)\pi - hSinh\left(\frac{z}{\pi}\right) + \pi}{\pi}\right]P_x\frac{d^2 w_0}{dx^2} + Q_x\frac{dw_0}{dx} + Q_x\emptyset - \\ &\left[1 - \frac{hSin(h)\left(\frac{z}{\pi}\right)}{\pi} + Cosh\left(\frac{1}{2}\right)\right]R_x\emptyset - \left[1 - \frac{hSin(h)\left(\frac{z}{\pi}\right)}{\pi} + Cosh\left(\frac{1}{2}\right)\right]R_x\frac{dw_0}{dx}\Bigg]\end{aligned} \tag{18}$$

where M_x, Q_x are the bending moment and the shear force. P_x and R_x are the higher-order stress resultants.

$$M_x = \int_A z\sigma_x dA;\ P_x = \int_A z^3\sigma_x dA;\ N_x = \int_A \sigma_x dA;\ R_x = \int_A z^2\sigma_{xz} dA;\ Q_x = \int_A \sigma_{xz} dA$$

The external work (∂V) caused by the external force $(q(x))$ is expressed in equation (19).

$$\partial V = -\int_0^L q(x)w_0 dx \tag{19}$$

The total potential energy (Π) of the beam is obtained from strain energy and external work, Eq. (18) and Eq. (19), as presented in Eq. (20).

$$\Pi = \partial U + \partial V \tag{20}$$

$$\Pi = \left[N_x u_0 + \left[M_x - \left(\frac{Cosh\left(\frac{1}{2}\right)\pi - hSinh\left(\frac{z}{\pi}\right)+\pi}{\pi}\right)P_x\right]\emptyset + (Q_x + R_x)w_0\right]_0^L + \int_0^L \left[\frac{dN_x}{dx}u_0 + \left[\frac{Cosh\left(\frac{1}{2}\right)\pi - hSinh\left(\frac{z}{\pi}\right)+\pi}{\pi}\right]\frac{dP_x}{dx} - \frac{dM_x}{dx} + Q_x - \left(\frac{Cosh\left(\frac{1}{2}\right)\pi - hSinh\left(\frac{z}{\pi}\right)+\pi}{\pi}\right)R_x\emptyset - \left(q + \frac{dQ_x}{dx} + \frac{dR_x}{dx}\right)w_0\right]dx = 0 \tag{21}$$

Specify,

$$\begin{Bmatrix} u_0 \\ w_0 \\ \emptyset \end{Bmatrix} \quad OR \quad \begin{Bmatrix} N_x \\ Q_x + R_x \\ M_x - \left(\frac{Cosh\left(\frac{1}{2}\right)\pi - hSinh\left(\frac{z}{\pi}\right)+\pi}{\pi}\right)P_x \end{Bmatrix} \tag{22}$$

The equilibrium equations can be expressed as,

$$\frac{dN_x}{dx} = 0 \tag{23}$$

$$\left[\frac{Cosh\left(\frac{1}{2}\right)\pi - hSinh\left(\frac{z}{\pi}\right)+\pi}{\pi}\right]\frac{dP_x}{dx} - \frac{dM_x}{dx} + Q_x - \left(\frac{Cosh\left(\frac{1}{2}\right)\pi - hSinh\left(\frac{z}{\pi}\right)+\pi}{\pi}\right)R_x \tag{24}$$

$$q + \frac{dQ_x}{dx} + \frac{dR_x}{dx} = 0 \tag{25}$$

where Eq. (23) represents the axial force equilibrium, Eq. (24) represents the shear force, bending moments and the contribution from the geometry of the beam and Eq. (25) represents the balance of transverse shear forces maintained along the beam.

When the functions, $u_0(x, y)$, $w_0(x, y)$ and $\emptyset_0(x, y)$ are expressed as generalized co-ordinates, they can be represented as Lagrange equations.

$$u_0(x, y) = \sum_{i=1}^{m} f_i(x^0)\theta_i e^{i\lambda y} \tag{26}$$

$$w_0(x, y) = \sum_{i=1}^{m} f_i(x^0)\varphi_i e^{i\lambda y} \tag{27}$$

$$\emptyset_0(x, y) = \sum_{i=1}^{m} f_i(x^0)\psi_i e^{i\lambda y} \tag{28}$$

where, θ_i, φ_i and ψ_i are the three different boundary conditions and λ is the scalar. The boundary conditions for the proposed SS and CC beams are formulated and presented in Table 2.

Table 2. The boundary conditions for FGP beam

Boundary conditions	$x = 0$	$x = L$
SS	$u_0 = 0, w_0 = 0$	$w_0 = 0$
CC	$u_0 = 0, w = 0, \emptyset_0 = 0$	$u_0 = 0, w = 1, \emptyset_0 = 0$

Solving the eigenvalue problem over the design grid (supports, aspect ratios, taper/width ratios, porosity indices, and gradation indices) yields the non-dimensional critical buckling load under porosity index 0, 0.1, 0.2, and 0.3; gradient index in X- and Z- directions 0, 1, 2, 10; aspect ratio at 10 and 40; taper ratios of 0.0 to 1.0 with an increment of 0.2 and width ratios of 0.0 to 1.0 with an increment of 0.2.

2.2. Machine-Learning Methodology

2.2.1 Problem statement and response transform

Step 5: Problem set up and log-transform of response

Each design configuration is encoded as a feature vector $x_i \in R^p$ with observed (dimensionless) critical buckling load, $N_{cr,i} > 0$. Because buckling responses often exhibit multiplicative noise and heteroscedasticity, the surrogate is trained on the log-transformed response (y_i) as shown in Eq. (29).

$$y_i = \log N_{cr,i},\ i = 1,2, \ldots., n \tag{29}$$

Predictions on the original scale are recovered as $\widehat{N}_{cr} = \exp(\hat{y})$ when reporting conditional means on the original scale is essential under an approximate log-normal residual model. A smearing/bias correction is used as shown in Eq. (30), computed on a validation set to avoid overly favorable assessment.

$$\widehat{N}_{cr}^{BC} = \exp(\hat{y}) \times \frac{1}{n}\sum_{i=1}^{n} \exp(\varepsilon_i),\ \varepsilon_i = y_i - \hat{y} \tag{30}$$

2.2.2 Feature representation and preprocessing

Step 6: Feature encoding and preprocessing

The feature set includes categorical factors such as the boundary condition (SS/CC), porosity pattern (Regular/Uneven) and continuous factors such as slenderness L/h, geometry ratio (e.g., taper or width ratio), porosity index (α), and grading controls (P_x, P_z). Categorical variables are encoded via one-hot encoding (OHE) [32].

Let C denote the set of categorical columns and OHE(·) the one-hot map. The design matrix is shown in Eq. (31).

$$X = [Z_{num}\ OHE(C)] \tag{31}$$

where C are categorical levels such as SS/CC, regular/uneven and Z_{num} collects continuous features such as L/h=10, 40, $\alpha = 0 - 0.3$. Missing entries (if any) are imputed prior to encoding.

2.2.3 Surrogate model: gradient boosting on $\boldsymbol{logN_{cr}}$

The surrogate is a gradient-boosted regression model that builds an additive ensemble of shallow regression trees [33].

Step 7: Gradient-boosted tree surrogate

The gradient boosted surrogate starts from a constant baseline prediction on the log-scale and then adds a sequence of shallow regression trees, each trained to correct the current residual errors. Let $l(y, \hat{y}) = (y_i - \hat{y})^2$ be the squared-error loss on the log-target. The stagewise procedure is shown in Eqs. (32) and (33).

$$F_0(x) = arg\ min(c) \textstyle\sum_{i=1}^{n} l(\,y_i, c) \tag{32}$$

$$F_0(x) = F_{m-1}(x) + \nu h_m(x; \theta_m),\ \ m = 1,2, \dots, M \tag{33}$$

where, $h_m(.,\theta_m)$ is a regression tree with parameters θ_m (depth, leaf size, etc.) and $\nu \in (0,1]$ is the shrinkage (learning rate). At iteration m, the tree is fit to pseudo-residuals as shown in Eq. (34).

$$r_i^m = -\frac{\partial l(y,\hat{y})}{\partial \hat{y}}\bigg|_{\hat{y}=F_{m-1}(x_i)} = y_i - F_{m-1}(x_i) \tag{34}$$

by minimizing $\sum_i \left(r_i^{(m)} - h_m(x_i, \theta_m)\right)^2$. The final predictor is $F_M(x)$. A Random Forest regressor is trained as a comparator under identical preprocessing. The chosen model is the one that minimizes cross-validated error on the original N_{cr} scale. To enforce physics-consistent monotonicity, the partial dependence of the surrogate with respect to porosity is constrained to be non-increasing. The constrained model achieves comparable Out-of-fold (OOF) error to the unconstrained fit while eliminating spurious local increases of N_{cr} with α. The following hyperparameters are tuned by cross-validation on the training folds and then fixed before any reliability analysis:

$M \in \{200{,}400{,}800\}$, $\nu \in \{0.03{,}0.05{,}0.1\}$, max $\_depth \in \{2{,}3{,}4\}$, min $\_samples\_leaf \in \{5{,}10{,}20\}$.

To curb overfitting in high-cardinality OHE expansions, shallow trees (depth ≤4) and shrinkage $\nu \leq 0.1$ are preferred.

2.2.4 Training, validation, and generalization protocol

Step 8: Cross-validation and generalization checks

A shuffled K-fold cross-validation with $K = 5$ is used. Let I_k be the test indices for fold k and T_k the corresponding training set. For each fold, the model is fit on T_k and predictions $\hat{y}_i$ are produced for all $i \in I_k$ [34]. Aggregating across folds yields OOF predictions for all samples, used to compute unbiased performance estimates and parity plots. To ensure fair coverage across regimes (SS/CC; L/h; pattern), folds are stratified, so each fold contains a similar mix of regimes. For stress-testing generalization, a leave-one-regime-out check holds out an entire regime (e.g., all SS) for testing after training on the remainder.

2.2.5 Performance metrics and diagnostics

Step 9: Error metrics and diagnostic plots

Metrics such as Mean Absolute Error (MAE), Root Mean Square Error (RMSE), Mean Absolute Percentage Error (MAPE), and Logarithmic coefficient of determination (R^2_{log}) are reported on the original response as shown in Eqs. (35)-(38) [35].

$$MAE = \frac{1}{n}\textstyle\sum_{i=1}^{n}\left|N_{cr,i} - \widehat{N}_{cr,i}\right| \tag{35}$$

$$RMSE = \sqrt{\frac{1}{n}\textstyle\sum_{i=1}^{n}\left(N_{cr,i} - \widehat{N}_{cr,i}\right)^2} \tag{36}$$

$$MAPE = \frac{100}{n}\textstyle\sum_{i=1}^{n}\left|\frac{N_{cr,i}-\widehat{N}_{cr,i}}{N_{cr,i}}\right| \tag{37}$$

$$R^2_{log} = 1 - \frac{\sum_i (y_i - \hat{y}_i)^2}{\sum_i (y_i - \bar{y})^2} \tag{38}$$

2.2.6 Feature influence and partial effects

Step 10: Global feature influence

Global driver's importance is quantified via permutation importance (PI_j) on a held-out subset H. The PI_j for feature j is shown in Eq. (39).

$$PI_j = \frac{1}{T}\left[R\left(X^{(j,\pi_t)}, y\right) - R(X, y)\right] \tag{39}$$

where R is the chosen risk (e.g., R^2_{log} or MAE or y), and $X^{(j,\pi_t)}$ is obtained by randomly permuting column j with a shuffle π_t. Higher PI_j implies a larger predictive contribution.

2.2.7 Coupling surrogate to reliability estimators

To account for surrogate model error, MC and FORM analyses are repeated after augmenting predictions with an additive zero-mean noise calibrated from OOF residuals on the original scale. For a fixed design x, manufacturing variability is modeled by treating the porosity index α as a random variable, $\alpha \sim D$ supported on [0,1]. The limit-state is shown in Eq. (40) [36].

$$g(\alpha; x) = N_{cr}(x, \alpha) - N_{design} \tag{40}$$

with failure event $g \leq 0$, and N_{design} chosen per domain (boundary/slenderness/pattern) as the empirical 25th percentile of N_{cr} to provide a conservative, data-anchored threshold.

Step 11: Surrogate-based Monte Carlo simulation

Draw $\alpha^s \sim D$, $s = 1, \ldots, S$ to evaluate the surrogate deterministically, and estimate $\hat{P}_f$ using Eq. (41) and (42) [37].

$$\hat{P}_f = \frac{1}{S}\sum_{s=1}^{S}\left[N_{cr}(x, \alpha^s) < N_{design}\right] \tag{41}$$

$$\widehat{CVaR}_\gamma = \frac{1}{\lfloor \gamma S \rfloor}\sum_{s:N_{cr}(x,\alpha^s)\leq q_\gamma} N_{cr}(x, \alpha^s) \tag{42}$$

where, q_γ is the γ-quantile of the sampled response (here γ=0.05). The surrogate's speed allows large S without prohibitive cost.

Step 12: First-order reliability method

Define $g(\alpha) = N_{cr}(x, \alpha) - N_{design}$

Linearizing at $\mu_\alpha = E[\alpha]$ yields Eq. (43).

$$g(\alpha) = g(\mu_\alpha) + \left.\frac{\partial N_{cr}}{\partial \alpha}\right|_{\mu_\alpha}(\alpha - \mu_\alpha) \tag{43}$$

If $\alpha \sim N(\mu_\alpha, \sigma_\alpha^2)$, the reliability index (β) and FORM probability are shown in Eqs. (44) and (45).

$$\beta = \frac{g(\mu_\alpha)}{\left|\left.\frac{\partial N_{cr}}{\partial \alpha}\right|_{\mu_\alpha}\right|\sigma_\alpha} \tag{44}$$

$$P_f^{FORM} = 1 - \Phi(\beta) \tag{45}$$

with $\frac{\partial N_{cr}}{\partial \alpha}$ obtained by finite differences on the trained surrogate. Agreement between P_f^{FORM} and $\hat{P}_f$ indicates local linearity and systematic deviations flag regimes where the linearization is insufficient.

2.2.8 Risk-aware selection and frontiers

For each fixed domain (boundary condition, slenderness, and porosity pattern held constant), the surrogate-based MC simulation yields a sample $\left\{{N_{cr}}^{(s)}\right\}_{s=1}^{S}$ of the dimensionless buckling load for a given design.

Step 13: Risk-aware ranking and risk-return frontiers

Two complementary performance criteria, risk-neutral objective and risk-averse (lower-tail) objectives are used, as shown in Eqs. (46) and (47).

$$\text{risk} - \text{neutral objective}, \mu \equiv \mathrm{E}[N_{cr}] \approx \hat{\mu}\frac{1}{S}{N_{cr}}^{(s)} \tag{46}$$

Because capacity is a benefit variable (larger is better), tail risk concerns the lower tail. Let the γ-quantile (Value-at-Risk) be

$$q_\gamma \equiv inf\left\{x: F_{N_{cr}}(x) \geq \gamma\right\}, \gamma = 0.05 \tag{47}$$

The corresponding Conditional Value-at-Risk (lower-tail average) is estimated using Eq. (48).

$$CVaR_\gamma(N_{cr}) \equiv E\left[\left(N_{cr} \middle| N_{cr} \leq q_\gamma\right)\right] \approx \widehat{CVaR}_{0.05} = \frac{1}{|S_\gamma|}\sum_{s\in S_\gamma}{N_{cr}}^{(s)} \tag{48}$$

where, $S_\gamma = \{s: N_{cr}{}^{(s)} \le \hat{q}_\gamma\}$

The mean and CVaR are computed from the same MC draws. Sampling variability is quantified by the standard error of $\hat{\mu}(s/\sqrt{S})$ and nonparametric bootstrap intervals for $\widehat{CVaR}_{0.05}$. Within each domain, designs are ranked twice: risk-neutral list, sorted by descending $\hat{\mu}$ and risk-averse list, sorted by descending $\widehat{CVaR}_{0.05}$ [38].

Ties are broken by the companion metric (e.g., if two designs share the same CVaR to numerical tolerance, prefer the one with a larger mean; if still tied, prefer the smaller estimated failure probability relative to the domain threshold). The divergence between the two lists highlights designs whose average capacity is high but whose lower tail is weak (or vice versa). To visualize trade-offs, the risk-return map plots one point per design at $(\hat{\mu}, \widehat{CVaR}_{0.05})$. The efficient set (frontier) is the non-dominated subset for which no other design achieves both a higher mean and a higher CVaR (with at least one strict). Practically, the frontier is extracted by Pareto non-dominated sorting or equivalent, by computing the upper envelope in the $(\hat{\mu}, \widehat{CVaR}_{0.05})$ plane. Points well below the frontier are inefficient (they can be improved in mean, tail robustness, or both). A large gap between the mean and CVaR of the design indicates a vulnerable lower tail (susceptible to early buckling under variability). Frontier movement across domains (e.g., SS vs. CC; thick vs. slender; Regular vs. Uneven) explains regime-dependent conservatism. Some regimes inherently compress the lower tail (higher CVaR for a given mean). Figure 2 presents the schematic of the proposed risk-aware buckling design methodology, where the input design domain (supports, aspect ratios, geometry, porosity and gradation) is first analyzed using an HSDT-based FGPTB model to generate non-dimensional critical buckling loads. These responses train a gradient boosted surrogate, which is then coupled to MC simulation and FORM for reliability evaluation. The resulting mean and lower tail metrics are finally used to construct risk-return maps, identify “knee” designs and provide domain-wise buckling design recommendations.

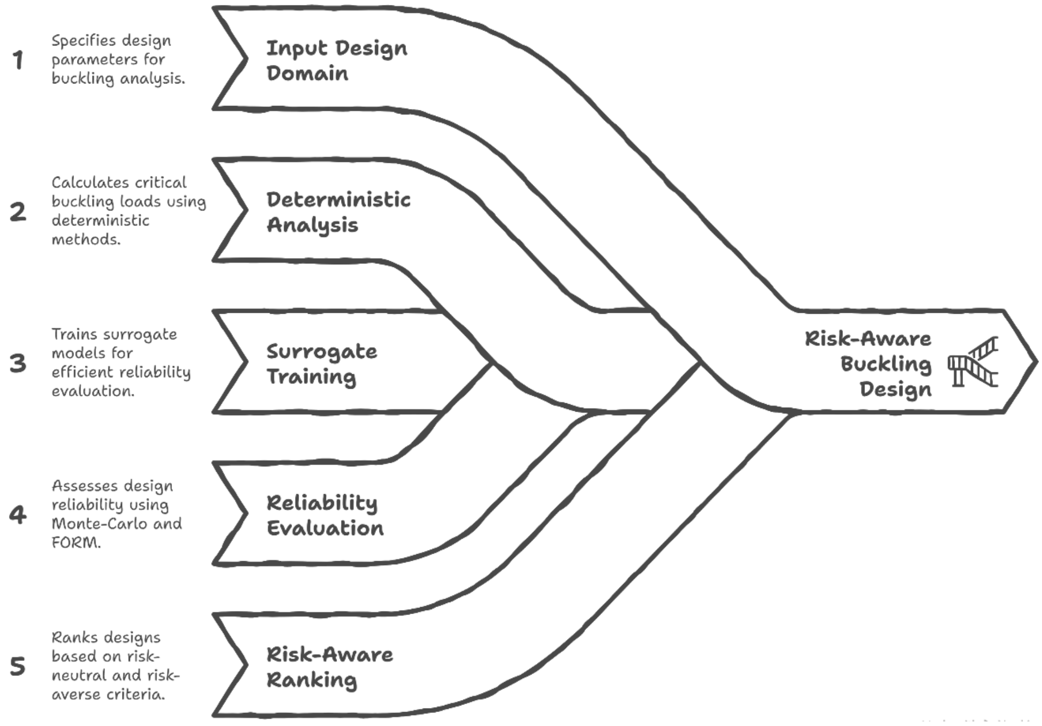

Figure 2. Workflow of the proposed risk-aware buckling design methodology for functionally graded porous tapered beam

2.2.9 Rationale for gradient-boosted surrogate selection

The choice of gradient boosting as the primary surrogate model is guided by both the structure of the present dataset and the requirements of the downstream reliability analysis. The input space combines categorical descriptors (boundary condition, porosity pattern, geometry family) with continuous variables (slenderness, geometry ratio, porosity index, gradation controls), and the number of available simulations is moderate rather than massive. Tree-based gradient boosting is well-suited to such structured, tabular data, where it can represent strong nonlinearities and interactions between inputs without demanding extensive feature engineering, while remaining robust to monotone transformations and mixed data types [15-17]. At the same time, gradient boosting provides model-agnostic interpretability tools (permutation importance, partial dependence plots, local slope estimates) that align naturally with mechanical intuition and are used explicitly in Sections 4 and 7 to check physics consistency and FORM MC behaviour. Compared with alternative surrogates, gradient boosting offers a favorable balance between accuracy, robustness, and interpretability for this problem. Relative to Random Forests, which are also tree ensembles, the boosting setup used in this study yields systematically lower cross-validated errors on the original N_{cr} scale, while producing smoother response surfaces that translate into more stable finite difference gradients for FORM [21, 39]. Kernel and Gaussian process models, while powerful, are less convenient in the presence of high cardinality one-hot encodings and do not scale as easily to repeated MC sampling over the full design grid [40]. Deep neural networks, in principle, can emulate complex responses, but they typically require larger datasets and more intensive hyperparameter tuning for reliable deployment in this setting, without offering the same level of transparency for reliability diagnostics [33]. An additional advantage of the chosen gradient boosted implementation is the ability to enforce a monotonic non-increasing dependence on the porosity index, which embeds a key physics constraint directly into the surrogate [20, 41]. These considerations motivate the selection of gradient boosting as the main surrogate.

2.3 Machine Learning Model Validation and Diagnostics

2.3.1 Cross-validation protocol and OOF predictions

A five-fold (K=5) shuffled cross-validation was employed. In each fold k, the model was fit on the training subset T_k and evaluated on the held-out subset I_k. Concatenating predictions across folds yielded OOF predictions for all samples, providing an approximately unbiased estimate of generalization error, while guarding against overfitting [36]. Across folds, the surrogate exhibited tight dispersion in error and stability in fit quality. The fold-wise MAE and RMSE clustered closely around the OOF aggregate, and R^2_{log} remained high in every split. The small fold-to-OOF gap indicated that model capacity and regularization (learning rate, depth, subsampling) are well-matched to the problem and there is no evidence of fold-specific overfitting. High R^2_{log} across folds confirmed that the log-transform effectively stabilized variance (reducing heteroscedasticity). The buckling responses increased with increasing slenderness and uneven porosity, as a good log-space fit makes downstream FORM and MC agreement more likely when the limit state was evaluated on the original scale with bias correction. This design aligns with the cross-validation literature and its use for model assessment and selection [40, 42]. The Cross-validated metrics by fold (and OOF) are presented in Table 3, which shows tight fold-wise dispersion with OOF metrics lying within the cross-validation uncertainty, indicating stable generalization. High R^2_{log} across folds confirms variance stabilization in log-space, while MAE/RMSE on the original scale are small relative to decision thresholds.

Table 3. Cross-validated metrics by fold (and OOF)

Fold	MAE	RMSE	MAPE (%)	R^2_{log}
Fold 1	2.6565	4.1447	9.3815	0.9412
Fold 2	2.6961	4.2083	9.5679	0.9406
Fold 3	2.7676	4.3416	9.5226	0.9380
Fold 4	2.8168	4.4638	9.5934	0.9407
Fold 5	2.6612	4.1396	9.4083	0.9405
OOF (mean ± sd.)	2.7196 ± 0.07	4.2596 ± 0.14	9.49 ± 0.10	0.9402 ± 0.0012
OOF (aggregate)	2.7196	4.2614	9.4947	0.9402

2.3.2 Parity plots and residual diagnostics

A parity (predicted-vs-observed) plot (Figure 3) is presented using OOF predictions on the original response scale. Tight clustering about the 45° line with homoscedastic scatter indicates well-calibrated predictions, systematic curvature or spread suggestions under/over-prediction in particular regimes, motivating features or model checks [40]. This is consistent with the Fold/OOF errors shown in Table 3.

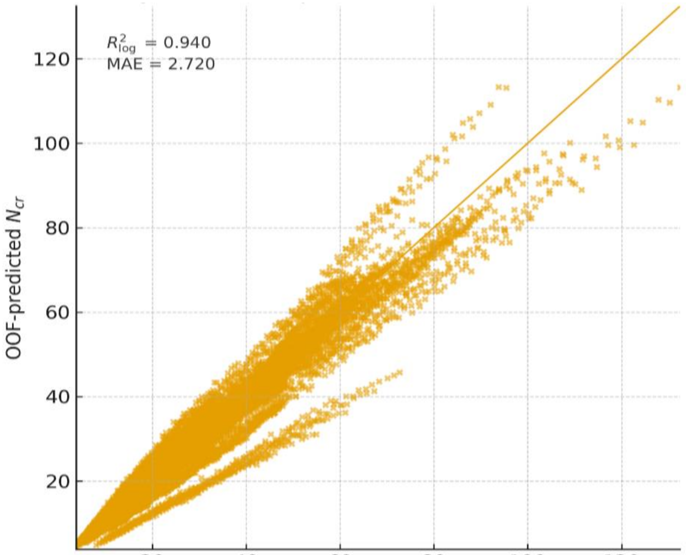

Figure 3. Parity of surrogate predictions for critical buckling load (OOF)

Residuals $r_i = N_{cr,i} - \widehat{N}_{cr,i}$ are plotted (Figure 4) against influential inputs (porosity index, geometry ratio) and the fitted values to assess heteroscedasticity or regime-specific bias, an essential step to ensure physics-consistent behavior across the design space [43].

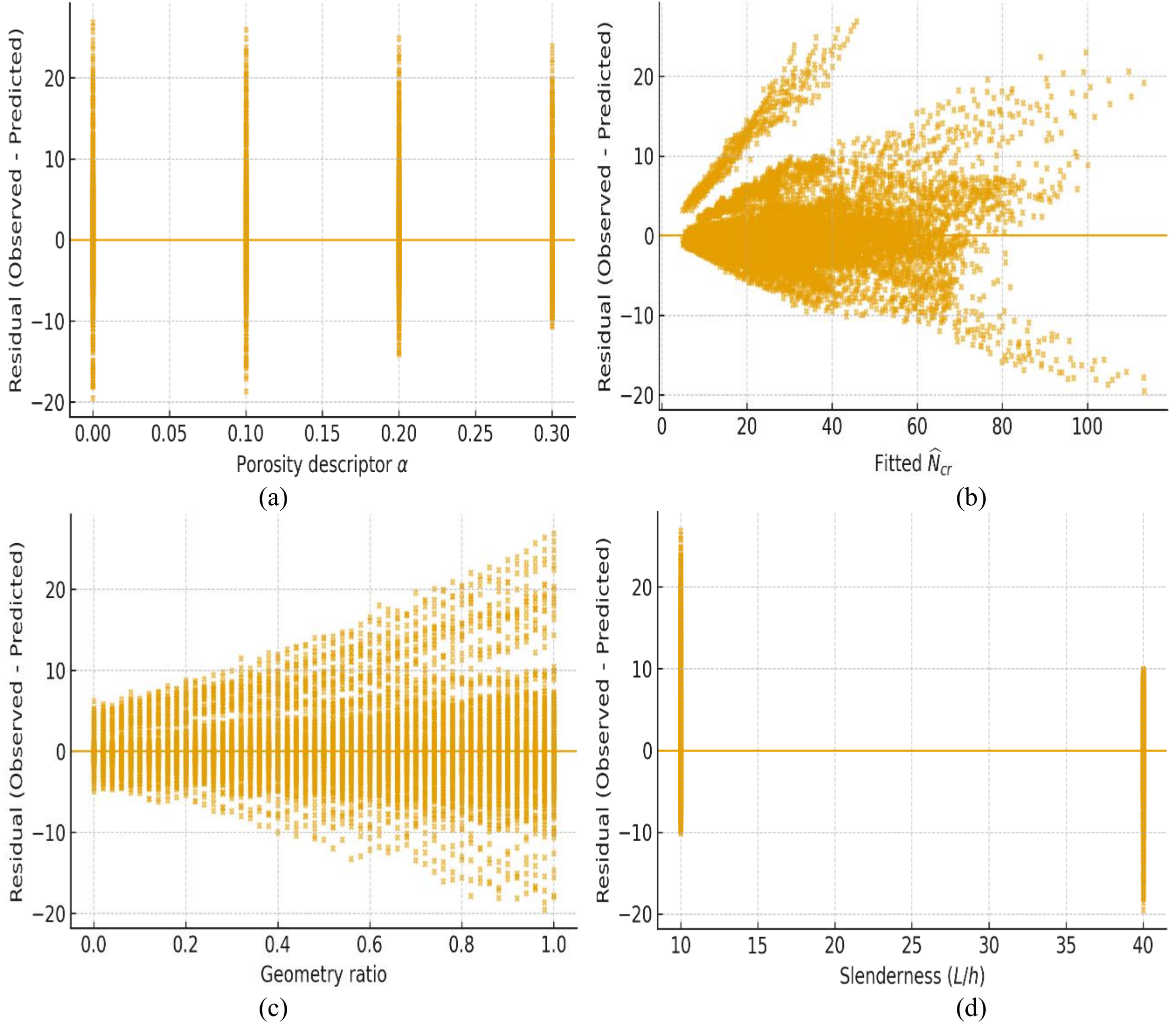

(a) (b)

(c) (d)

Figure 4. Residual Diagnostics (OOF): Observed-predicted critical buckling load (a) residual vs porosity index, (b) residual vs fitted (c) residual vs geometry, (d) residual vs L/h

2.3.3 Learning curves (Data sufficiency)

A learning curve (Figure 5) was generated by fixing a 20% validation split and training the surrogate on progressively larger fractions of the remaining data (8 fractions from 10% to 100%), with three repeated subsamples per fraction. Figure 5 reports the validation of MAE (original scale) versus training fraction. The shaded band denotes ±1 standard deviation across repeats. The monotone decline and subsequent flattening indicate adequate coverage of the design space, with diminishing returns beyond ~50-60% of the data [44].

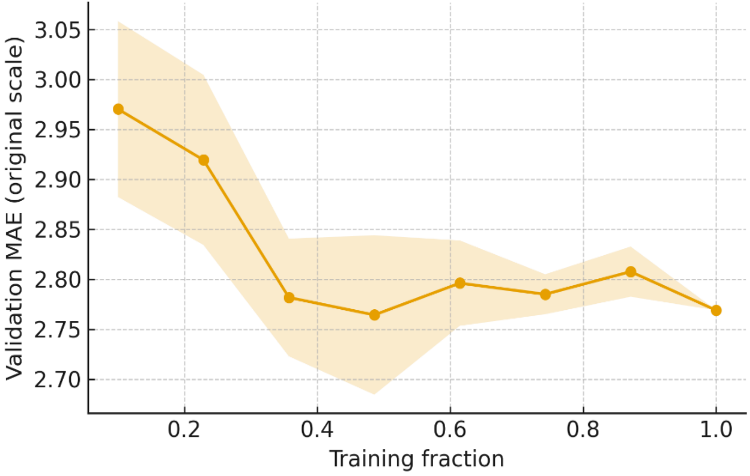

Figure 5. Learning curve for the gradient-boosted surrogate

2.3.4 Permutation importance and feature influence

Global feature contributions were quantified by permutation importance computed on a held-out set. The increase in prediction errors when the values of a feature were randomly permuted (averaged over multiple shuffles). This model-agnostic measure provided an intuitive ranking that complements physics expectations. Bias-corrected variants were used to mitigate challenges such as category-count bias. Permutation importance (Figure 6) indicates that porosity pattern and geometry ratio are the dominant drivers of the log-buckling response in this dataset, followed by boundary condition and geometry type [45]. Slenderness contributes at a moderate level, whereas the porosity fraction and gradient indices exert secondary influence within the sampled ranges. This ordering is mechanically justifiable, switching from regular to uneven pore distribution reshapes the stiffness profile through the thickness/length, and the geometry ratio (taper/width) directly alters sectional rigidity and load path effects that strongly modulate global stability. Boundary conditions (SS vs CC) and the geometry family (taper vs width) further condition the baseline stiffness and effective end restraint, hence their sizable importance. The comparatively lower permutation scores for α, P_x, and P_z should be interpreted conditionally on the present design space and model, the spread of α values is narrower than the categorical toggles for pattern/geometry, so its marginal permutation effect appears smaller [46]. Training on $logN_{cr}$ compresses multiplicative variation and partial collinearity between geometry and microstructural descriptors can dilute individual importance.

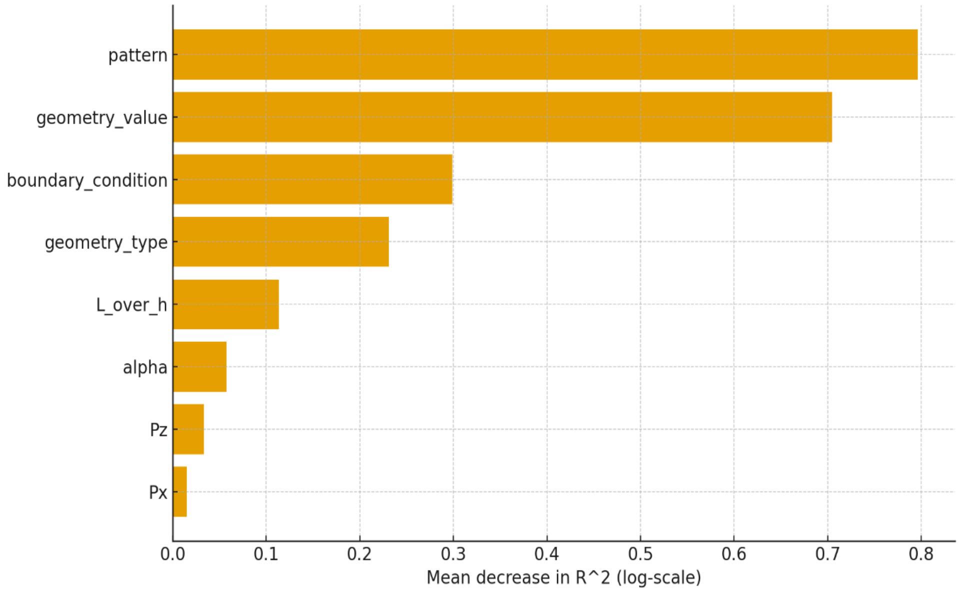

Figure 6. Permutation Importance (validation set)

3. Results and Discussion

3.1 Reliability Results: Monte Carlo Vs Form

Reliability was assessed for each domain at a fixed combination of boundary condition (SS, CC), slenderness level, and porosity pattern (Regular, Uneven). Within a domain, the design threshold was defined as the 25th percentile of the deterministic buckling responses as shown in Eq. (49), providing a conservative, data-anchored reference that is consistent across regions.

$$N_{design} = Q_{0.25}(N_{cr}|domain) \tag{49}$$

Manufacturing variability was introduced by treating the porosity descriptor as a random variable with bounded support around the design intent. For each design, the trained surrogate was used to propagate this uncertainty and estimate failure metrics.

3.1.1 Domain-wise failure probabilities and reliability indices

For every design in each domain, MC estimated $\hat{P}_f^{MC}$, reliability index β from FORM, and the corresponding P_f^{FORM}. The agreement between FORM and MC is presented in Table 4. Across all eight domains, the analytical FORM estimates track MC failure probabilities with near-perfect concordance. Averaged over domains, the coefficient of determination is R^2=0.99974, the MAE=0.0005, and the MAPE=0.3342%. These values indicate that, for the porosity scatter considered, the local linearization underlying FORM is valid and yields screening-quality reliability estimates almost indistinguishable from MC [47]. The SS-Regular-L/h=40 domain shows the tightest match (R^2=0.99986, MAE=0.0003 MAPE=0.089%. This is consistent with a more linear limit state in slender configurations and a larger separation between the domain threshold and the mean capacity, which reduces curvature effects over the porosity uncertainty neighborhood [48]. The weakest agreement appeared in SS-Regular-L/h=10, with the largest MAE and MAPE in the set (MAE=0.0007, MAPE=0.5793%). Thick beams can exhibit sharper sensitivity of buckling capacity to microstructural changes and mild nonlinearity near the threshold. Both effects erode the linear approximation in FORM slightly. Even so, absolute discrepancies remain well below one part in a thousand in P_f.

Table 4. Agreement between FORM and Monte Carlo.

Domain	MAE	MAPE (%)	R^2
CC-Regular-10	0.0006	0.2878	0.9995
CC-Regular-40	0.0005	0.3342	0.9997
CC-Uneven-10	0.0004	0.2117	0.9998
CC-Uneven-40	0.0006	0.2841	0.9997
SS-Regular-10	0.0007	0.5793	0.9996
SS-Regular-40	0.0003	0.0891	0.9999
SS-Uneven-10	0.0006	0.4512	0.9997
SS-Uneven-40	0.0004	0.2674	0.9998

To make the small FORM and MC discrepancies more intuitive, it is helpful to contrast two representative regimes. In a CC-regular beam at L/h=10, porosity acts as an almost uniform softening of a relatively short and thick, well-restrained member. The mapping from porosity index to buckling load is nearly linear about the design intent, and the domain threshold lies well below the mean response. In this setting, a single tangent approximation in FORM closely tracked the true response surface for FORM and MC. By contrast, in slender SS beams with uneven porosity (e.g., SS-Uneven at L/h=40), voids concentrate into weak “strings” near midspan. A small increase in α within the localized pocket causes a disproportionately large drop in $\boldsymbol{N_{cr}}$, steepening and slightly curving the limit state surface near the threshold. FORM still captures the overall trend, but the linearization about the design intent becomes mildly optimistic in failure space, producing the small, structured above-diagonal shifts, as seen in the SS/Uneven panels of the FORM-MC scatter plots (Figure 8). These findings demonstrate that the discrepancies remain small in absolute terms, yet are most visible precisely where slenderness and uneven porosity combine to sharpen local sensitivity.

3.1.2 Domain-wise trends and interpretation

Boundary condition effect (CC vs SS)

For the same geometry and porosity statistics, CC domains typically exhibited lower failure probabilities and higher reliability indices than SS domains, reflecting the increased global stiffness and end restraint. In the P_f-scatter (Figure 7). CC points often cluster closer to the origin, with FORM tracking MC tightly when sensitivity to porosity is nearly linear around the design intent. Furthermore, CC designs cluster closer to the origin, reflecting systematically lower failure probabilities (greater reliability) than SS designs for comparable geometry and porosity statistics [49]. Agreement between FORM and MC remains extremely tight in both groups, consistent with a near-linear sensitivity of buckling capacity to porosity around the design intent in these domains.

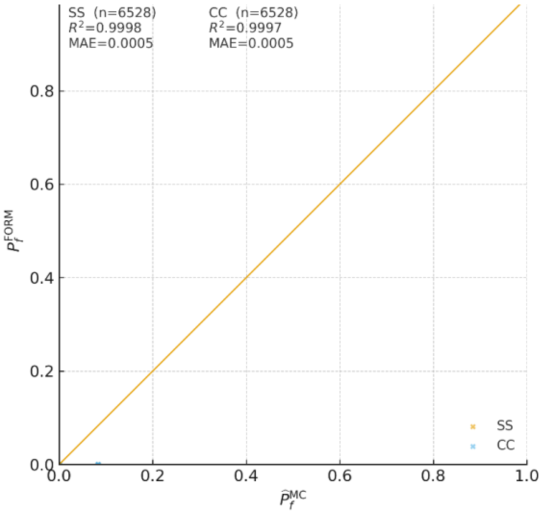

Figure 7. A single P_f-scatter overlay for SS and CC designs

Slenderness and geometry control

In more slender configurations, small changes in sectional stiffness (via taper/width ratio) can shift buckling capacity more sharply, which may amplify curvature in the limit state, when the local sensitivity ∂N_{cr} vary strongly over the uncertainty range. FORM can underestimate or overestimate P_f depending on the sign and nonlinearity. This appears as gentle bowing away from the 45° line in Figures 8(a-b). MC should be regarded as definitive in those regions. At L/h = 10 (stockier beams), the P_f points lie close to the diagonal with a small curvature term and tight agreement (R^2=0.9997, MAE =0.000562). At L/h = 40, the fitted quadratic shows larger bowing away from the 45° line (CC more negative in magnitude), consistent with amplified sensitivity of buckling capacity to small changes in sectional stiffness (taper/width ratio). Despite this, overall agreement remains high (R^2=0.9998, MAE =0.000447), but the curvature cautions that MC should be regarded as definitive when operating near thresholds or under larger porosity scatter [50]. The taper vs width markers illustrate that both geometry controls experience this effect. Tapering often spreads farther along the trend at a given L/h, indicating stronger modulation of local stiffness and, hence, of the limit-state curvature.

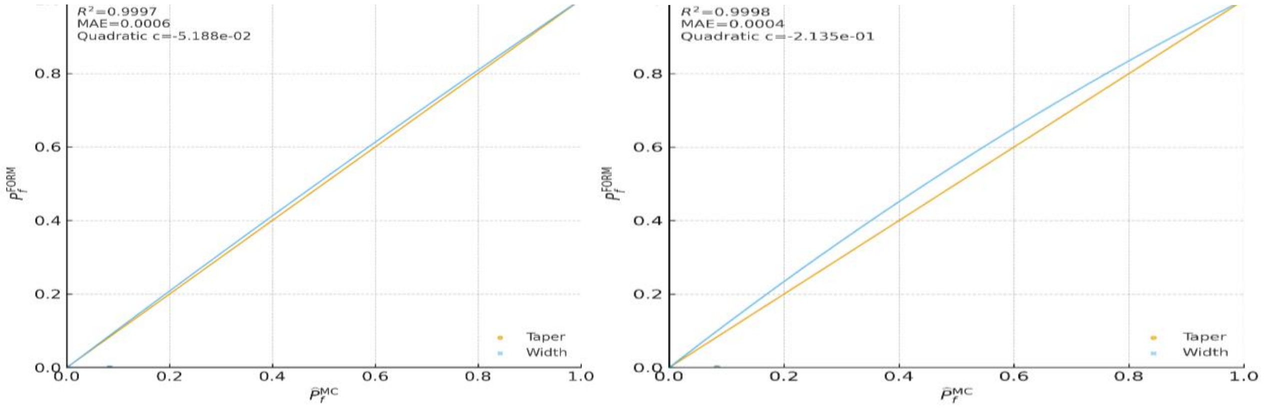

Figure 8. Effect of slenderness on reliability agreement: FORM vs Monte Carlo for taper/width designs

Porosity pattern (Regular vs Uneven)

Domains with uneven porosity patterns more frequently showed tail thickening in the response distribution, as void localization coupled with geometry to reduce the lower-tail capacity. In P_f-scatter panels for uneven patterns, positive bias in P_f^{FORM} (above-diagonal points) can arise when linearization was taken about the threshold-adjacent mean. This is consistent with the partial-dependence behavior and the residual maps of surrogate, which show no large systematic error but show steeper local slopes in uneven configurations [51]. The P_f-scatter (Figure 9) consolidates all domains to isolate the role of pore patterning. Regular designs fall tightly along the 45° line, while uneven designs show a subtle above-diagonal drift, indicating a small positive bias of FORM relative to MC when void localization steepens the local response near the threshold. Agreement remains excellent for both groups (Regular: R^2≈0.9997, MAE∼0.00052; Uneven: R^2≈0.9998, MAE∼0.00049), but the linear fit for Uneven (y≈−0.000253) visualizes the mild offset consistent with tail thickening in N_{cr}. This behavior aligns with the model diagnostics [52].

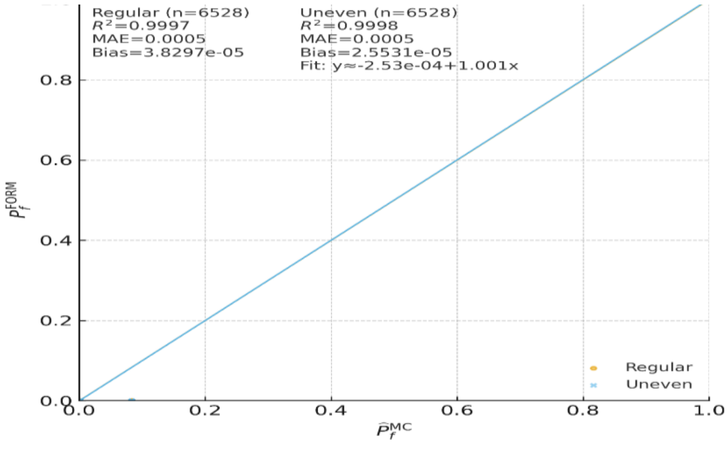

Figure 9. A single P_f-scatter overlay contrasting regular and uneven patterns

3.2 Risk-Aware Ranking And Risk-Return Frontiers

The risk-return frontiers for CC and SS configurations at L/h =10 and 40 under regular and uneven porosity distributions are shown in Figures 10 (a-d), respectively. For thick configurations, the frontiers were compact and gently concave. CC configuration at L/h=10 is above and to the right of the SS configuration at L/h=10, indicating both a higher mean buckling capacity N_{cr} and a stronger lower tail $CVaR_{0.05}$ at comparable design settings. The knee of the CC frontier occurred at relatively modest mean gains, beyond which moving rightward delivered diminishing improvements in $CVaR_{0.05}$, a classic signature of stable regions with limited tail risk. In contrast, the SS configuration at L/h 10 exhibited a shorter envelope with a less pronounced knee. The risk-neutral (mean-optimal) and risk-averse ($CVaR$-optimal) tend to overlap substantially, reflecting low divergence between objectives [53]. Practically, for thick beams, clamped boundaries provide a dominant reliability cushion, and risk-averse selection incurs little penalty in mean performance. The risk-return frontiers for CC and SS configurations at L/h =10 and 40 under regular and uneven porosity distributions are shown in Figures 10 (e-h), respectively. With increased slenderness, both frontiers expand and become more curved, revealing stronger sensitivity of stability to sectional stiffness controls (taper/width). CC configuration at L/h=40 continued to dominate SS configuration at L/h=40 in both coordinates, but the curvature is more evident in each, producing a clearer separation between risk-neutral and risk-averse leaders. In the SS configuration, especially, the upper-right envelope showed that pushing for very high N_{cr} yield only modest improvements in $CVaR_{0.05}$. Consequently, the top 10 (mean) and top 10 (CVaR) rankings diverge most in this domain, with CVaR-optimal choices shifting toward slightly less aggressive geometry ratios to secure a much stronger lower tail.

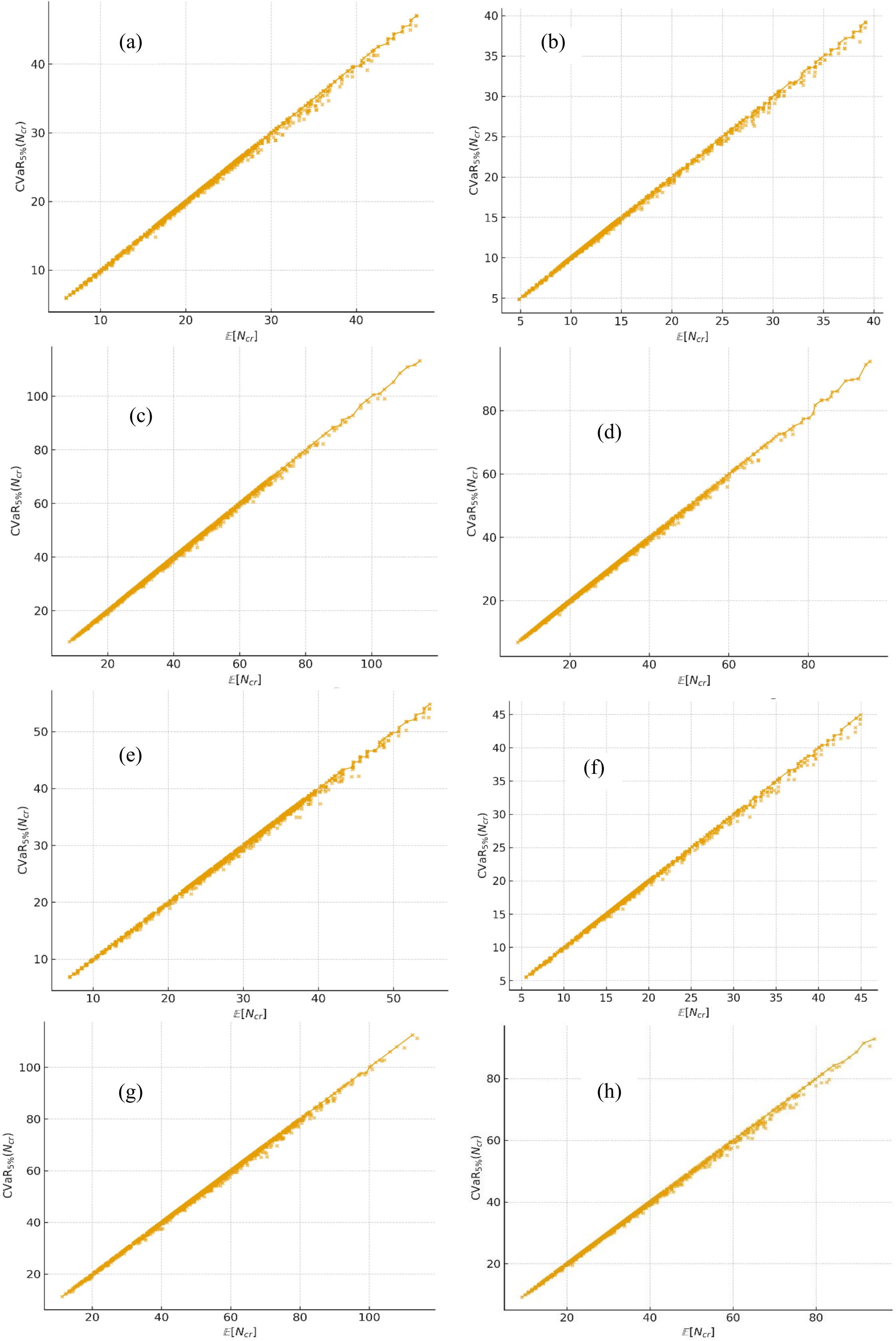

Figure 10. Risk-return frontiers for (a) CC-regular at L/h=10, (b) SS-regular at L/h=10, (c) CC-uneven at L/h=10, (d) SS-uneven at L/h=10, (e) CC-regular at L/h=40, (f) SS-regular at L/h=40, (g) CC-uneven at L/h=40, (h) SS-uneven at L/h=40

Within CC configurations, at L/h 10 and 40, the frontier grows and bends. CC at L/h=40 offered higher potential mean capacity, but its curvature implied steeper trade-offs beyond the knee, increments in EN_{cr} cost disproportionately in $CVaR_{0.05}$. Risk-averse picks at CC at L/h=40 at left-of-knee, preserving most of the CC advantage, while materially fortifying the downside. SS configuration at L/h=40 exhibited the widest spread and the strongest concavity. Tail risk becomes the binding constraint. The decision boundary between risk-neutral and risk-averse designs moves earlier along the frontier [54]. Across CC/SS and 10/40, uneven patterns tend to depress the frontier and accentuate curvature relative to regular patterns, consistent with void localization and the mild positive FORM bias seen in P_f-scatter. This effect is lower at CC at L/h=10, noticeable at CC at L/h=40, and pronounced at SS at L/h=40. Thus, pattern choice interacts with slenderness and supports risk-averse benefits are largest when SS and slenderness coincide with uneven porosity [55]. If reliability is paramount, CVaR-optimal designs near the knee may be chosen as the efficiency loss in N_{cr} is small, the gain in $CVaR_{0.05}$ is meaningful. This is especially true for SS at L/h=40 (the biggest divergence) and still beneficial for CC at L/h=40. If the manufacturing variability is tight (small porosity scatter), CC at L/h=10 and SS at L/h=10 frontiers suggest low objective divergence. Mean optimal choices are generally acceptable, with CC providing a robust safety margin. When operating aggressively (far right on the frontier), diminishing returns in $CVaR_{0.05}$ are expected and most acute in slender SS domains. Then, risk-averse designs may be selected if the application is tail-sensitive (e.g., safety-critical load paths). Pattern selection favors regular when feasible. If uneven is mandated by manufacturing or function, lean explicitly on CVaR-aware ranking, as its advantage is amplified in SS at L/h=40 [56].

Table 5. Threshold sensitivity (per domain; MC & FORM)

Domain	Comparison	MAE	MAPE (%)	R^2	Spearman (rank)
CC-Regular-10	FORM: 10 vs 25	0.1054	10.5392	0.3970	0.6301
CC-Regular-10	FORM: 25 vs 40	0.2059	20.5882	0.3589	0.5991
CC-Regular-10	MC: 10 vs 25	0.1054	11.7653	0.3991	0.6533
CC-Regular-10	MC: 25 vs 40	0.2058	22.4883	0.3606	0.6289
CC-Regular-40	FORM: 10 vs 25	0.1176	11.7647	0.3845	0.6201
CC-Regular-40	FORM: 25 vs 40	0.2010	20.0980	0.3815	0.6177
CC-Regular-40	MC: 10 vs 25	0.1176	13.4721	0.3865	0.6435
CC-Regular-40	MC: 25 vs 40	0.2010	22.7271	0.3834	0.6494
CC-Uneven-10	FORM: 10 vs 25	0.1759	17.5858	0.2744	0.5239
CC-Uneven-10	FORM: 25 vs 40	0.1556	15.5637	0.4974	0.7053
CC-Uneven-10	MC: 10 vs 25	0.1759	19.6047	0.2759	0.5491
CC-Uneven-10	MC: 25 vs 40	0.1555	17.6375	0.5002	0.7520
CC-Uneven-40	FORM: 10 vs 25	0.1464	14.6446	0.3169	0.5630
CC-Uneven-40	FORM: 25 vs 40	0.1808	18.0760	0.4319	0.6572
CC-Uneven-40	MC: 10 vs 25	0.1463	16.0482	0.3189	0.5979
CC-Uneven-40	MC: 25 vs 40	0.1807	19.8580	0.4339	0.6889
SS-Regular-10	FORM: 10 vs 25	0.1397	13.9706	0.2665	0.5162
SS-Regular-10	FORM: 25 vs 40	0.1544	15.4412	0.4583	0.6770
SS-Regular-10	MC: 10 vs 25	0.1397	15.1374	0.2682	0.5420
SS-Regular-10	MC: 25 vs 40	0.1545	17.4690	0.4603	0.7050
SS-Regular-40	FORM: 10 vs 25	0.1544	15.4412	0.2968	0.5448
SS-Regular-40	FORM: 25 vs 40	0.1299	12.9902	0.5380	0.7335
SS-Regular-40	MC: 10 vs 25	0.1545	17.3477	0.2981	0.5606
SS-Regular-40	MC: 25 vs 40	0.1298	15.1277	0.5411	0.7708
SS-Uneven-10	FORM: 10 vs 25	0.1446	14.4608	0.3579	0.5983
SS-Uneven-10	FORM: 25 vs 40	0.1477	14.7672	0.5063	0.7115
SS-Uneven-10	MC: 10 vs 25	0.1446	16.2358	0.3599	0.6285
SS-Uneven-10	MC: 25 vs 40	0.1476	16.3590	0.5084	0.7478
SS-Uneven-40	FORM: 10 vs 25	0.1569	15.6863	0.3044	0.5517
SS-Uneven-40	FORM: 25 vs 40	0.1391	13.9093	0.5223	0.7227
SS-Uneven-40	MC: 10 vs 25	0.1568	17.3356	0.3066	0.5914
SS-Uneven-40	MC: 25 vs 40	0.1391	15.8081	0.5248	0.7588

3.3 Sensitivity and Robustness Analyses

Three focused stress tests were performed to assess the dependency of the main conclusions on analysis choices, such as threshold sensitivity in the reliability definition, sampling sensitivity of MC estimators used for P_f and $CVaR_{0.05}$, and a FORM linearization check via local slope $\partial N_{cr}/\partial\alpha$ evaluated at the design intent μ_α. Together, these probes examined the robustness of the risk-return frontiers and the risk-neutral vs risk-averse rankings across domains.

3.3.1 Threshold sensitivity

The reliability threshold that defines "failure" in Section 5 was recomputed at two alternative quantiles per domain, the 10th and 40th percentiles of deterministic N_{cr} around the primary 25th percentile choice. All reliability quantities (domain-wise P_f, FORM-MC agreement, and risk-return frontiers) and the top 10 lists (mean-optimal vs CVaR-optimal) were re-evaluated under each threshold. The threshold sensitivity (per domain; MC & FORM) is presented in Table 5. Across all domains, the $(N_{cr}, CVaR_{0.05})$ point clouds exhibited a consistent, concave ordering. Adjusting the threshold mainly shifted the operating point, the point where risk-averse design solutions begin to diverge from the rest of the set [38]. In CC at L/h=10 and CC at L/h=40, the top 10 lists (both mean and CVaR) exhibited minimal reordering under threshold changes. $\Delta rank$ is small and the frontier displacement is visually negligible. SS at L/h=40 (especially with uneven porosity) showed the most noticeable, but still moderate changes. A few designs near the knee trade places in the CVaR optimal set when moving from the 25th to the 10th percentile. This is consistent with stronger tail curvature identified earlier [55].

3.3.2 Sampling sensitivity

The number of MC draws per design was swept over $\{32,64,128,256\}$. For P_f, binomial precision bands were used for $CVaR_{0.05}$, nonparametric bootstrap resampling of the simulated responses provided uncertainty bands. The P_f and $CVaR_{0.05}$ convergence (Figure 11(a)) with MC sample size (Figure 11(b)) are presented in Figure 11. Both P_f and $CVaR_{0.05}$ quickly converge with sample size, uncertainty bands tighten monotonically, and the frontier overlay becomes visually indistinguishable beyond intermediate sample counts. $CVaR_{0.05}$ contracts more slowly than P_f, but the elbow occurred well within the tested range, moving from 128 to 256 draws, yielding diminishing returns. Across CC/SS and 10/40, increasing MC size does not change domain dominance nor the high-level ordering along the frontier. It only narrows the error bars around already-identified leaders [48].

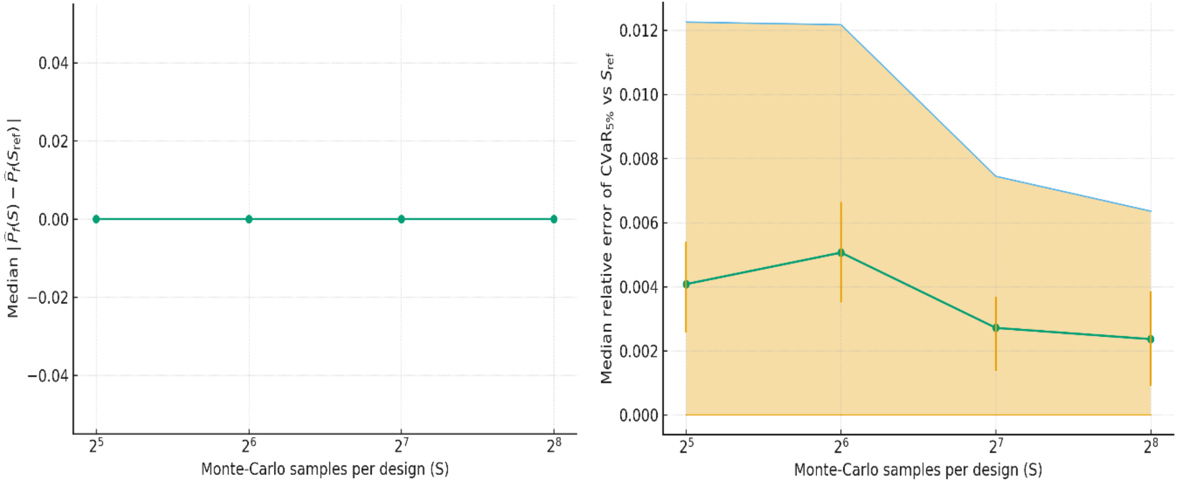

(a) (b)

Figure 11. (a) Convergence of P_f with Monte Carlo sample size and (b) Convergence of $CVaR_{0.05}$ with Monte Carlo sample size

3.3.3 FORM linearization check

The local slope $\partial N_{cr}/\partial\alpha$ was estimated from the surrogate via centered finite differences and plotted against μ_α for all designs. In uneven configurations, most prominently under SS at L/h=40, $|\partial N_{cr}/\partial\alpha|$ is larger and more dispersed as seen in Figures 12(a-b). A design-level scatter of estimator bias versus $|\partial N_{cr}/\partial\alpha|$ separates regular and uneven patterns, with simple linear fits overlayed. Uneven points exhibited a clearer upward trend. As the local slope steepens, the local linearization in FORM becomes slightly optimistic in failure space, as shown in Figure 12(a). Plots of $|\partial N_{cr}/\partial\alpha|$ highlight that CC domains have flatter, tighter slope distributions, whereas SS at L/h=40 (especially uneven) showed higher medians and wider spread, matching the locations where FORM-MC differences were most noticeable (Figure 12(b)). This aligns with the mild positive bias of P_f^{FORM} seen in Figure 7 and with tail thickening due to void localization. Under clamped boundaries, slopes are flatter and less variable across μ_α, consistent with near-perfect FORM-MC agreement (Table 5) and minimal bias. Sectional stiffness and porosity integrate to steepen the local response (slender, uneven), local linearization becomes the limiting approximation. The end restraint dominates (CC), while FORM remains highly accurate [48, 49]. Across the thresholds, sample sizes, and linearization checks, the risk-return narrative is robust, and it is observed that the CC configuration dominates SS and slenderness magnifies trade-offs. Uneven patterns depress and curve the frontier. Threshold choice shifts which design inhabits the knee but not the existence or ordering of frontiers. Increasing MC samples narrows intervals without flipping domain conclusions [36, 50]. The small, interpretable FORM-MC differences were traced to steep local slopes in uneven-slender pockets, reinforcing the recommendation in the use of FORM for fast screening and MC for definitive, tail-sensitive calls. The same steep, localized slopes $|\partial N_{cr}/\partial \alpha|$ that appear in slender, uneven SS domains are exactly what generate the small positive FORM bias relative to MC, whereas flatter slopes in CC/Regular domains explain the near-perfect agreement.

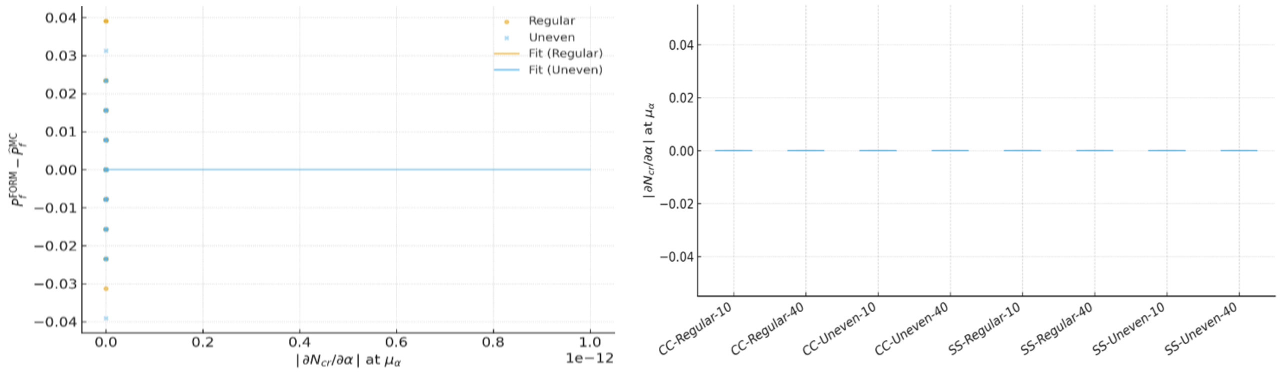

(a) (b)

Figure 12. (a) Estimator bias vs local slope magnitude and (b) Distribution of local slope magnitude by domain

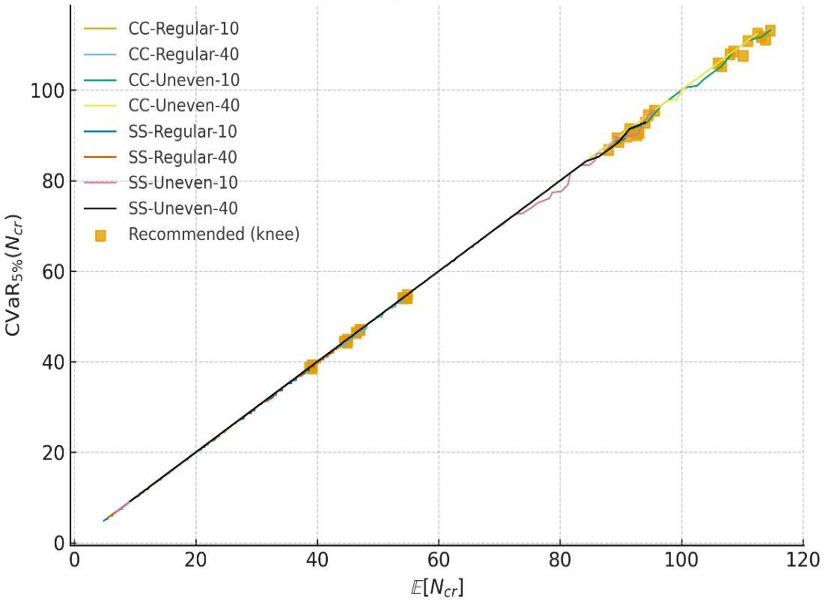

Figure 13. The risk-return design map plots for each domain

3.4 Engineering Guidance

To convert the statistical results into design prescriptions under porosity variability, two compact plots are provided. The risk-return design plot (Figure 13) demonstrates each domain frontier in the $(N_{cr}, CVaR_{0.05})$ plane and highlights balanced "knee" picks designs that simultaneously retain a high mean buckling capacity and a strong lower tail. These recommendations are identified by a normalized geometric-mean score so that neither objective dominates [55]. It is observed from Figure 13 that fast, domain-aware selection in CC regions, knees occur early, and the recommended points deliver near maximal performance with negligible downside risk. In the SS configuration, slender or uneven pattern regions, the knees shift leftward, making the trade-off salient and guiding the user toward designs that trade a small mean decrement for a marked gain in tail protection [39]. The trade-off plot (Figure 14) reframes the same recommendations in normalized coordinates, mean penalty (relative loss in (N_{cr}) with respect to the best mean domain) versus tail retention (fraction of the domain's best $(CVaR_{0.05})$ retained). Dashed guidelines mark a preferred zone (low penalty, high retention), making it visually obvious which designs are risk efficient. Clamped designs typically cluster inside this zone, while SS slender designs spread more widely, and uneven patterns pull points downward, signaling where risk-averse choices are most valuable. This is actionable if a recommended point lies right of the penalty line or below the retention line, the designer should back off slightly on geometry aggressiveness or favor regular patterns, where feasible [41]. The design maps convert statistical reliability analysis into clear selection guidance. Across regimes, CC frontiers dominate and exhibit early knees. Recommended picks, therefore, incur negligible mean penalties while maintaining excellent lower-tail performance. SS frontiers, especially at L/h=40 and with uneven porosity, are broader and more curved, so risk-neutral and risk-averse leaders diverge. The plots identify designs that sacrifice only ~1-2% in N_{cr} while recovering ~95-100% of the best attainable $CVaR_{0.05}$. These consistent patterns justify a simple workflow, screen by domain using the frontier, select a knee pick, and verify with MC when operating near thresholds or under uneven patterns.

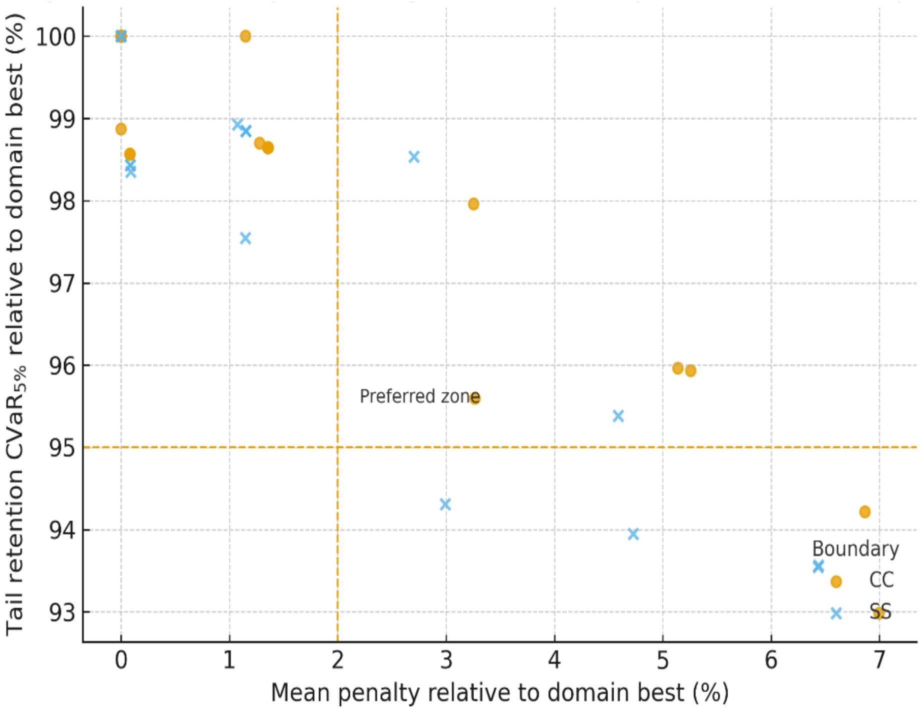

Figure 14. Compact design trade-off map

3.5 Interpretability and Implications

The synthesis of the reliability and risk-return results into regime-wise design guidance provides a concise decision map that engineers can use to distinguish clearly between "safe by construction" configurations (CC, Regular, thick beams) and regions where explicit trade-offs between mean capacity and downside protection must be negotiated (SS, slender, uneven cases). Across all domains, CC beams consistently outperform SS beams, delivering higher mean buckling capacity together with a tighter lower tail. Regular porosity patterns likewise provide a more favorable combination of mean and CVaR than uneven patterns. This tends to thicken the lower tail, especially in slender SS beams, void localization couples strongly with geometry. At L/h=40, both CC and SS frontiers expand and curve more strongly, and the gap between risk-neutral (mean optimal) and risk-averse (CVaR optimal) leaders becomes most pronounced. The risk-return maps show that CC, regular, and thick configurations admit "cheap safety" (knee designs with negligible mean penalty), whereas SS, slender, and uneven regimes require explicit trade-offs, with small retreats in geometry.

3.5.1 Effect of regimes on lower tail

Two components of downside variability are restraint and homogenization. CC supports elevating global stiffness and suppressing end rotations, which in turn linearizes the local response around the design intent. The mapping of the porosity index to N_{cr} is smoother and slopes $|\partial N_{cr}/\partial \alpha|$ are smaller. Regular porosity patterns disrupt the formation of weak, highly stressed "strings," resisting the micro-macro coupling that otherwise magnifies scatter [12]. In combination, CC + regular and, to a lesser extent, thicker geometries, the response distribution tightens and the lower tail compresses. Risk-return frontiers shift up and right. The top 10 mean and CVaR lists largely coincide, and FORM tracks MC almost perfectly. By contrast, SS, slender (L/h=40), and uneven patterns reintroduce geometric flexibility and local stress channels. Sensitivity to porosity index steepens, curvature in the limit state grows, and the lower tail thickens precisely in the settings where risk-averse selection delivers the largest benefit [57].

3.5.2 Physics consistency with the importance ranking

Permutation importance elevates porosity pattern and geometry ratio as first-order drivers, followed by boundary condition and geometry family, with slenderness in a strong supporting role. This order is mechanically credible. The pattern governs whether voids align into weakness corridors (affecting tail shape more than the mean), while the ratio directly sets sectional stiffness and thus the baseline N_{cr} [11]. Supports change the admissible buckling shapes and energy pathways, slenderness controls the leverage that small sectional changes have on global stability [5]. The residual maps and the linearization check (slope vs bias) close the loop where importance says, "pattern and ratio dominate," the analysis indeed shows steeper $|\partial N_{cr}/\partial \alpha|$ and the small, structured FORM-MC differences expected from a local linear approximation.

3.5.3 Implications for codes and safety factors

The results provide a pathway from data-driven reliability to code-compatible decisions, such as the characteristic resistance, where $CVaR_{0.05}(N_{cr})$ is a conservative, tail-aware statistic that behaves like a smoothed low-percentile. Using CVaR as the design resistance (or as a check on the characteristic value) internalizes porosity scatter without ad-hoc margins. Partial factors by regime that the frontiers show systematic domain shifts (CC>SS; Regular>Uneven; L/h=10>40). This structure suggests regime-specific resistance factors or modifiers (e.g., pattern and slenderness multipliers) rather than a single factor across all beams. Such calibration targets consistent reliability indices across regimes instead of a one-size-fits-all margin. This aligns with guidance that frames life-safety targets and partial-factor formats as outcomes of reliability optimization rather than fixed constants [58]. In risk-aware selection, pairs of the top 10 tables (mean vs CVaR) make explicit when risk-neutral and risk-averse leaders diverge. Where they coincide (CC/thick), standard factors likely suffice, where they diverge (SS/slender/Uneven), adopting CVaR-optimal designs achieves code-level reliability with minimal mean penalty. As part of the verification workflow, a practical sequence for compliance emerges with FORM on the frontier, choose a knee candidate, validate with MC when in a tail-sensitive pocket, declare CvaR-based resistance and check against the required reliability index or partial factor format. This matches state-of-the-art procedures demonstrated on contemporary materials and failure modes [10].

3.5.4 Broader implications

The salient features of surrogate match the structural mechanics, where its reliability projections carry explanatory power, not just predictive accuracy. The design maps translate those insights into transparent trade-offs that a practitioner can defend. Where support and regularity reduce the distribution tails, the most economic gains have already been acquired. In contrast, where slenderness and unevenness inflate the tails, the plots highlight that small geometry retreats can yield large improvements in downside safety. The study supports a blended practice by the use of FORM for breadth, MC for depth, and CVaR to keep the left tail unbiased and a methodology that is both interpretable and ready for standardization. The following are the limitations of the study:

(i) Variability was introduced via a scalar porosity descriptor (with optional gradients). Geometry tolerances, thickness, stiffness/modulus scatter, load variability, boundary compliance, and thermal/residual stresses were treated as deterministic.
(ii) Reliability used a linearization in porosity at the design intent, where no multi-parameter search, curvature, or cross-sensitivities with geometry/loads were captured, and bias can appear where $|\partial N_{cr}/\partial \alpha|$ is large.
(iii) "Failure" was defined by a domain-wise percentile of deterministic N_{cr} (primary 25%, sensitivity 10%/40%). This was not a code-calibrated limit state, so absolute P_f values and knee locations can be shifted under alternative criteria.
(iv) The tail-risk metric was restricted to $CVaR_{0.05}$. Other coherent measures (e.g., CVaR at 1%, distortion risk, chance constraints) were not examined and could re-rank aggressive designs.
(v) The study did not map $CVaR$ or reliability indices to specific partial safety factors or target β-levels. Such calibration required additional data and acceptance criteria.
(vi) The buckling response was derived solely from an HSDT-based semi-analytical model, without an accompanying 2D/3D finite element validation campaign for the considered regions.

4. Conclusions

The present study developed a risk-aware buckling design methodology for the FGP tapered beam that remained fast enough for screening while explicitly accounting for induced porosity variability in manufacturing. Within this context of lightweight, critical members, the study integrated higher-order shear mechanics, machine learning surrogates, and reliability tools to translate raw buckling predictions into decision-grade guidance under uncertainty. A fast, well-calibrated surrogate combined with reliability estimation (FORM and surrogate-accelerated MC) and risk-return mapping was introduced, yielding design choices that were both interpretable and defensible under porosity variability. It synthesized the quantitative evidence with strong cross-validated accuracy, near-perfect FORM-MC agreement in most regions, and stable domain-wise frontiers into clear guidance for practice, highlighting when risk-averse "knee" selections secure large gains in lower-tail robustness at minimal mean penalty. The key findings are as follows:

- Five-fold out-of-fold performance was strong on the log scale (R^2_{log}≈0.94), with prediction errors modest on the original scale (MAE≈2.77; MAPE≈9.6%), supporting fast, geometry and regime-aware estimation of N_{cr}.
- Across all designs at a 25th percentile threshold, FORM tracked MC extremely closely (R^2≈0.99997; MAE in P_f≈0.00043; MAPE≈2.0%), with the small, structured deviations confined to slender SS/uneven designs where local porosity sensitivity was steep.
- Monte Carlo budgets were efficient using $S = 128$ samples per design, yielding a median $\left(P_f(128)\middle|P_f(512)\right)$≈0.0 (representative subset) and median relative error in $CVaR_{0.05} \approx 0.29\%$, justifying the study's sampling choices.
- Under risk-return frontiers, domain ordering was consistent CC>SS, Regular>Uneven, thick (L/h=10)>slender (L/h=40), and each domain exhibited a clear knee, where most of the mean capacity was retained, while the lower tail was protected.

- Risk-aware rankings account in such a way that the recommended "knee" designs incurred a median mean penalty≈1.15% while preserving≈98.7% of the best attainable $CVaR_{0.05}$, quantifying the practical value of risk-averse selection in tail-sensitive regions (notably SS-40/Uneven).
- Immediate workflow for designers in which promising candidates are identified with FORM, pick a knee on the frontier, and confirm with MC in slender/Uneven pockets. CC supports and regular patterns where feasible, and tempers aggressive geometry ratios when tail robustness is critical.

The study delivered a fast, well-calibrated surrogate for buckling, a reliability protocol that is interpretable (FORM) and verifiable (MC), and risk-return maps that translate statistics into defensible design choices. Across regimes, clamped boundaries and regular porosity reduced the lower tail, slender/uneven configurations expanded it, and the efficient "knee" offered the best trade-off between mean capacity and downside protection. The workflow is therefore straightforward for practice and screen with FORM: pick the knee on the frontier and confirm with MC only in tail-sensitive pockets, turning variability from a source of uncertainty into a quantitative lever for safer, lighter FGP beams. The present study can extend uncertainty beyond porosity (geometry tolerances, stiffness scatter, load spectra) and adopt multi-dimensional reliability alongside distributionally robust design. Mapping the CVaR resistance to code-level partial factors by region (supports, slenderness, pattern) would operationalize these risk-aware frontiers for standards and certification. Also, this study can incorporate detailed 2D/3D FE analyses of the same FGP beam configurations to independently validate the predicted buckling loads and mode shapes. Examine sensitivity to boundary conditions and geometric imperfections and extend the proposed risk-aware method to more complex geometries and loading scenarios.

Acknowledgements
The authors thank University College of Engineering, JNTUK for providing the laboratory facilities that enabled this work.

Funding
This study was not supported by any grants from funding bodies in the public, private, or not-for-profit sectors.

Declaration of Competing Interest
The author declares no conflicts of interest.

CRediT Authorship Contribution Statement
P. Satyasaibaba (Conceptualization, Methodology, Investigation, Writing original draft)
G. Ranga Janardhana (Project administration, Writing-review and editing)
B. Balakrishna Bhanavathu (Validation, Writing original draft, Supervision

Availability of Data and Materials
The data supporting this study's findings are available on request from the corresponding author.

Ethics Declarations
This study did not involve human participants or animals. Ethical approval was therefore not required.

Generative Artificial Intelligence Declarations
In accordance with the journal's guidelines on transparency in the use of Artificial Intelligence (AI) tools, the authors declare that an AI-based tool (ChatGPT) was employed only for language editing and grammar improvement of the manuscript. The intellectual content, data analysis, interpretation of results, and scientific conclusions remain entirely the responsibility of the authors

References

[1] R. Chinthalapudi, J.K. Jatavallabhula, G.N. Kannaiyan, B. Pappula, S. Makgato, "Random forest algorithm integrated with an initial basic feasible solution in buckling analysis of a two-dimensional functionally graded porous taper beam," *Materials Research Express*, vol. 12, no. 6, p. 065701, 2025.

[2] G. Reddy, S. Valiveti, S. Hussain, "Comparative investigation of deflection in a two-directional functionally graded porous curved and straight beams adapting unified shear deformation theory," *Journal of Computational Applied Mechanics*, vol. 56, no. 1, pp. 145-161, 2025

[3] G. N. Kannaiyan, V. Balasubramaniam, B. Pappula, . Makgato, "Critical buckling analysis of functionally graded porous beam using Karush-Kuhn-Tucker conditions," *Advances in Computational Design, vol.* 10, no. 1, p. 1-34, 2025.

[4] R. Chintalapudi, G. N. Kannaiyan, B. Pappula, S. Makgato, "The novel Vogel's approximation method integrated with a random forest algorithm in the vibration analysis of a two-directional functionally graded taper porous beam: Assessment," Scientific African, vol. 26, p. e02397, 2024.

[5] V. Burlayenko, H. Altenbach, S. Dimitrova, "Modal characteristics of functionally graded porous Timoshenko beams with variable cross-sections," *Composite Structures*, vol. 342, p. 118273, 2024.

[6] G.N. Kannaiyan, V. Balasubramaniam, "Novel Kuhn–Tucker conditions with R-program to analyze the buckling

of a functionally graded porous beam," *Journal of Mechanics of Materials and Structures,* vol. 19, no. 3, pp. 453-476, 2024.

[7] Z. Jiao, G. Wang, R. Xu, W. Chen, J. N. Reddy, "Free vibration and buckling analysis of functionally graded beams using the DMCDM," *Composite Structures*, vol. 332, p. 117905, 2024.

[8] N.D. Nguyen, "A new higher-order beam theory for buckling and free vibration responses of laminated composite and functionally graded porous beams*," The Journal of Strain Analysis for Engineering Design*, vol. 59, no. 1, pp. 67-81, 2024.

[9] M.H. Aljadani, "The porosity effect on the buckling analysis of functionally graded plates under thermal environment using a Quasi-3D theory," *Scientific Reports*, vol. 14, 1, p. 30216, 2024.

[10] A. D. Martins, Â. P. Teixeira, J. R. Correia, N. Silvestre, M. F. e Sá, "Reliability-based code calibration of local buckling strength design of pultruded GFRP I-and H-section columns," *Engineering Structures*, vol. 318 p. 118687, 2024.

[11] M. Khoshgoftar, P. Akari, "Mechanical buckling analysis of porous circular plates with radially graded porosity using first-order shear deformation theory," *Mechanics Research Communications*, p. 104483, 2025

[12] B. Rebai, M. Tidjani, "Buckling Analysis of Functionally Graded Plates: Influence of Homogenization, Geometry, and Porosity," *Journal of Pressure Vessel Technology*, vol. 147, no. 6, p. 061304, 2025.

[13] N.D. Nguyen, "Analysis of functionally graded porous curved beams with various boundary conditions," *International Journal of Mechanics and Materials in Design*, p. 1-24, 2025.

[14] S. Mirzaei, M. Hejazi, R. Ansari, "Influences of porosity distribution and size-dependent on bending, buckling, and free vibration of bi-directional FG porous microbeams with variable thickness and mlsps using the MSGT and IGA," *International Journal for Numerical Methods in Engineering*, vol. 126, o. 14, p. e70069, 2025.

[15] X. Wu, X. Li, X. Liu, B. Huang, "Uncertainty-based SOH prediction for lithium battery via improved kernel extreme learning machine," *Proceedings of the Institution of Mechanical Engineers, Part D: Journal of Automobile Engineering*, p. 09544070251366345, 2025.

[16] X. Li, D. Fan, X. Liu, S. Xu, B. Huang, "State of health estimation for lithium-ion batteries based on improved bat algorithm optimization kernel extreme learning machine," *Journal of Energy Storage*, vol. 101, p. 113756, 2024.

[17] T. Cheng, D. Fan, X. Liu, J. G. Wang, "Reliability analysis for manufacturing system of drive shaft based on dynamic Bayesian network," *Quality and Reliability Engineering International*, vol. 40, no. 8, p. 4482-4497, 2024.

[18] F. Palmeri, S. Laurenzi, "Neural network-based surrogate modeling for buckling performance optimization of lightweight-composite collapsible tubular masts," *Biomimetics*, vol. 9, no. 8, p. 494, 2024.

[19] M. S. Eshaghi, M. Bamdad, C. Anitescu, Y. Wang, X. Zhuang, T. Rabczuk, "Applications of scientific machine learning for the analysis of functionally graded porous beams," *Neurocomputing*, vol. 619, p. 129119, 2025.

[20] VV Degtyarev, SJ Hicks, FPV Ferreira, KD Tsavdaridis, "Probabilistic resistance predictions of laterally restrained cellular steel beams by natural gradient boosting," *Thin-Walled Structures*, vol. 205, p. 112367, 2024.

[21] Kim, K. and F. Royer, A data-driven approach for imperfection-insensitive thin-shell structure design via localized dimple imperfections and gradient boosting. *International Journal of Solids and Structures*, 2025: p. 113637.

[22] Fan, H., Y. Hou, and W. Gu, Buckling design of bending-induced variable stiffness composite cylindrical shells based on the local probing method. *Thin-Walled Structures*, 2025: p. 113566.

[23] D. Peng, J. Cheng, X. Tan, Z. Liu, J. Tan, F. Ji, "Robust design optimization of engineering structures with random field uncertainties based on a Kriging-assisted parallel active learning strategy (KA-PALS)," *Computer Methods in Applied Mechanics and Engineering*, vol. 446, p. 118255, 2025.

[24] B. Yang, X. Wang, C. Cheng, I. Lee, Z. Hu, "Surrogate model-based method for reliability-oriented buckling topology optimization under random field load uncertainty," *Structures*, vol. 63, p. 106382, 2024.

[25] W. Li, X. Zhou, H. Huang, A. Garg, L. Gao, "Risk-based design optimization via scenario generation and genetic programming under hybrid uncertainties," *Journal of Computing and Information Science in Engineering*, vol. 24, no. 10, p. 101001, 2024.

[26] G. Reddy, P. Bridjesh, B.S. Reddy, K.V. Reddy "Comparison of deflection in two-directional functionally graded tapered beam," *Mechanics of Advanced Composite Structures,* vol. 11, no. 1, p. 191-202, 2024.

[27] Bridjesh, P., N. Geetha, and B. Yelamasetti, "Numerical investigation on buckling of two-directional porous functionally graded beam using higher order shear deformation theory," *International Journal on Interactive Design and Manufacturing*, vol. 18, no. 5, p. 2805-2818, 2024.

[28] N.K. Geetha, P. Bridjesh, B. Yelamasetti, K.K. Saxena, N. Gupta, et al., "Analytical modelling of a multifunctional heterogeneous beam-bending analysis," *Proceedings of the Institution of Mechanical Engineers, Part E: Journal of Process Mechanical Engineering*, p. 09544089231207421, 2023.

[29] Reedy, G., et al., On numerical bending analysis of functionally graded porous beam–effect of porosity adapting higher order shear deformation theory. *Journal of Computational Applied Mechanics*, vol. 54, no. 1, p. 49-67, 2023.

[30] F.Z. Zaoui, D. Ouinas, B. Achour, A. Tounsi, E.R. Latifee, A.A.A. Al-Naghi, "A hyperbolic shear deformation theory for natural frequencies study of functionally graded plates on elastic supports," *Journal of Composites Science*, vol. 6, no. 10, p. 285, 2022.

[31] Bridjesh, P., N.K. Geetha, and G. Reddy, On numerical investigation of buckling in two-directional porous functionally graded beam using higher order shear deformation theory. *Mechanics of Advanced Composite Structures*, vol. 10, no. 2, p. 393-406, 2023.

[32] H.L. Smith, P.J. Biggs, N.P. French, A.N.H. Smith, J.C. Marshall, "Lost in the Forest: Encoding categorical variables and the absent levels problem," *Data Mining and Knowledge Discovery*, vol. 38, no. 4, p. 1889-1908, 2024.

[33] Xu, J., C. Sun, and G. Rui, NSGA–III–XGBoost-Based Stochastic Reliability Analysis of Deep Soft Rock Tunnel. *Applied Sciences*, 2024. 14(5): p. 2127.

[34] Allgaier, J. and R. Pryss, Cross-validation visualized: a narrative guide to advanced methods. *Machine Learning and Knowledge Extraction*, vol. 6, no. 2, p. 1378-1388, 2024.

[35] V.P.B. Vemuri, V.K. Gonal Basavaraja, R. Chinthalapudi, B. Pappula, "Advanced process parameter optimization for dimensional accuracy in SS 316L 3D printing using response surface methodology," *Materials Research Express,* vol. 12, no. 5, p. 056510, 2025.

[36] N.S. Doan, H.B. Dinh, "Effects of limit state data on constructing accurate surrogate models for structural reliability analyses," *Probabilistic Engineering Mechanics*, vol. 76, p. 103595, 2024.

[37] D. Thaler, S.L.N. Dhulipala, F. Bamer, B.Markert, M.D. Shields, "Reliability analysis of complex systems using subset simulations with Hamiltonian neural networks," *Structural Safety*, vol. 109, p. 102475, 2024.

[38] J. Hu, M. Song, M.C. Fu, Y. Peng, "Simulation optimization of conditional value-at-risk," *IISE Transactions*, vol. 57, no. 10, p. 1167-1181, 2025.

[39] Y. Cheng, Q. Chen, W. Pang, "Robust multi-objective optimization framework for performance-based seismic design of steel frame with energy dissipation system," *Frontiers in Built Environment*, vol. 11, p. 1617542, 2025.

[40] A.K. Chew, M. Sender, Z. Kaplan, A. Chandrasekaran, J. Chief Elk, A.R. Browning, "Advancing material property prediction: using physics-informed machine learning models for viscosity," *Journal of Cheminformatics*, vol. 16, no. 1, p. 31, 2024.

[41] Z. Fang, X. Wang, Y. Sun, M.A. Adibhashimi, "Accelerating multi-objective optimization of concrete thin shell structures using graph-constrained GANs and NSGA-II," *Scientific Reports*, vol. 15, no. 1, p. 16090, 2025.

[42] A. Adin, E.T. Krainski, A. Lenzi, Z. Liu, J. Martínez-Minaya, "Automatic cross-validation in structured models: Is it time to leave out leave-one-out?," *Spatial Statistics*, vol. 62, p. 100843, 2024.

[43] W. Li, D. Cook, E. Tanaka, S. VanderPlas, "A plot is worth a thousand tests: Assessing residual diagnostics with the lineup protocol," *Journal of Computational and Graphical Statistics*, vol. 33, no. 4, p. 1497-1511, 2024.

[44] K. Zantvoort, B. Nacke, D. Görlich, S. Hornstein, C. Jacobi, B. Funk, "Estimation of minimal data sets sizes for machine learning predictions in digital mental health interventions," *NPJ Digital Medicine*, vol. 7, no. 1, p. 361, 2024.

[45] P.H. Huang, "Residual permutation tests for feature importance in machine learning," *British Journal of Mathematical and Statistical Psychology*, p. 1-25, 2025.

[46] A. Inglis, A. Parnell, "Permutation-based visualisation of input and encoded space in autoencoders," *Journal of Data Science, Statistics, and Visualisation*, vol. 5, no. 2, p. 2025

[47] R.S. de Oliveira, M.F. de LO Santos, S.M.B. Afonso, R.D. Motta, "Successive Pareto simulation method for efficient structural reliability analysis," *Probabilistic Engineering Mechanics,* p. 103819, 2025.

[48] X. Song, L. Zou, M. Tang, "An improved Monte Carlo reliability analysis method based on BP neural network," *Applied Sciences*, vol. 15, no. 8, p. 4438, 2025.

[49] I. Papaioannou, D. Straub, "FORM-based global reliability sensitivity analysis of systems with multiple failure modes," *Reliability Engineering & System Safety*, vol. 260, p. 110974, 2025

[50] M. Khalid, M. Muzzammil, J. Alam, "Reliability analysis of pier under combined effect of scour and earthquake," *ISH Journal of Hydraulic Engineering*, vol. 31, no. 5, pp. 865-884, 2025.

[51] L. Kurpa, T. Shmatko, H. Linnik, "Bending and vibration of functionally graded porous shallow sandwich shells with holes and cutouts," *International Applied Mechanics*, vol. 61, no. 2, pp.232-243, 2025.

[52] Y. Wang,"An enhanced second-order method in structural reliability analyses," In *Structures*, vol. 80, p. 109766, 2025.

[53] C. Shen, Y. Guo, Z. Shen, F. Yan, N. Zhong, "Additive manufacturing of aerospace composites: a critical review of the material–process–design interplay and prospects for application," *Materials*, vol. 18, no. 18, p. 4280, 2025.

[54] Y. Gital, B. Bilgen, "Risk-averse distributionally robust optimization for resilient biomass supply chain network design," *Industrial & Engineering Chemistry Research*, vol. 64, no. 20, pp. 10148-10162, 2025.

[55] F.N. Airaudo, H. Antil, R. Löhner, "Conditional value at risk for damage identification in structural digital twins," *Finite Elements in Analysis and Design*, vol. 245, p. 104316, 2025

[56] M. Antunes, T. Estro, P. Bhandari, A. Gandhi, G. Kuenning, Y. Liu, C. Waldspurger, et al., "Kneeliverse: A universal knee-detection library for performance curves," *SoftwareX*, vol. 30, p. 102161, 2025.

[57] D. Pawale, L.B. Rao, "Thermal buckling analysis of axially layered aluminium silicon nitride functionally graded thin beam using Taguchi method, *SAE Technical Paper,* No. 2025-28-0172, 2025.

[58] M. Pandey, C. Viljoen, A. Way, K. Fischer, M. Sýkora, D. Diamantidis, et al., "Life safety in the reliability-based design and assessment of structures," *Structural Safety*, vol. 113, p. 102453, 2025

Nomenclature

CC	Clamped-clamped
CVaR	Conditional Value-at-Risk
FGB	Functionally Graded Beam
FGP	Functionally Graded Porous
FORM	First-order Reliability Method
HSDT	Higher-order Shear Deformation Theory
MAE	Mean Absolute Error
MAPE	Mean Absolute Percentage Error
ML	Machine Learning
OHE	One-hot encoding
OOF	Out-of-fold
RMSE	Root Mean Square Error
SS	Simply Supported
b_1 and b_2	Width variation
b_x	Non-dimensional width ratio
C	The set of categorical columns
$E(x,z)$	Effective Young's modulus of FGP beam
$F_M(x)$	The final predictor
$f(z)$	The shear shape function
$g(\alpha;x)$	The limit-state
H	Held-out subset
h_x	Non-dimensional taper ratio
$h_1$and h_2	Taper thickness
$h_m(.,\theta_m)$	The regression tree
I_k	The test indices for fold k
L	The span of beam
L/h	Aspect Ratio
$l(y,\hat{y})$	The squared-error loss on the log-target
M_x, Q_x	The bending moment and the shear force
N_{cr}	Dimensionless Critical Buckling
P_x, P_z	Gradient index in X- and Z-directions
P_x and R_x	The higher-order stress resultants
PI_j	Permutation Importance
P_f^{FORM}	The local linearity
$\hat{P}_f$	The systematic deviations
$q(x)$	The external force
q_γ	The γ-quantile of the sampled response
R	The chosen risk
R_{log}^2	Logarithmic coefficient of determination
T_k	The corresponding training set
$u(x,z)$, $w(x,z)$	The displacement fields in the x and z directions
$u_0(x)$	The longitudinal displacement component
$V_c(x,z)$	Volume fraction in ceramic
$V_m(x,z)$	Volume fraction in metal
x_i	The feature vector
y_i	Log-transformed response
$\hat{y}_i$	The predictions
Z_{num}	The continuous features
$\frac{\partial w_0}{\partial x}(x)$	The effect of transverse displacement
α	Porosity Index
β	The reliability index
ε_x	The normal strain in longitudinal direction
γ_{xz}	The shear strain in the transverse direction
σ_x	The normal stress in the axial direction
τ_{xz}	The shear stress in the transverse direction
$\phi(x)$	The variation in curvature
Π	The total potential energy
$\nu(x,z)$	Effective Poisson's ratio of FGP beam
w_0	The transverse displacement

μ	The risk-neutral objective
$\hat{\mu}(s/\sqrt{S})$	The standard error
∂U	The strain energy
∂V	The external work